



ELSEVIER

Nuclear Instruments and Methods in Physics Research A 489 (2002) 469–495

**NUCLEAR  
INSTRUMENTS  
& METHODS  
IN PHYSICS  
RESEARCH**  
Section A

www.elsevier.com/locate/nima

# Perturbed $\gamma$ – $\gamma$ correlations from oriented nuclei and static moment measurements. II: $g$ factors at low spin and high spin

Martyn P. Robinson, Andrew E. Stuchbery\*

*Department of Nuclear Physics, Research School of Physical Sciences and Engineering, The Australian National University,  
Canberra, ACT 0200, Australia*

Received 26 November 2001; received in revised form 22 February 2002; accepted 26 February 2002

## Abstract

The perturbations of  $\gamma$ – $\gamma$  directional correlations from nuclei oriented by heavy-ion induced reactions, as observed with a multidetector array, are employed to measure the magnetic dipole moments of sub-nanosecond excited states in neutron-deficient nuclei. The technique is compared with other techniques for measuring  $g$  factors of short-lived excited states. Some representative results, which use transient hyperfine fields to measure  $g$  factors at high spin and static hyperfine fields to measure  $g$  factors at low spin, are presented. © 2002 Elsevier Science B.V. All rights reserved.

*PACS:* 21.10.Ky; 23.20.En; 27.50.+e; 27.70.+q

*Keywords:* Perturbed directional correlations from oriented nuclei; DCO; Nuclear moments;  $g$  factors

## 1. Introduction

In a previous paper [1] the formalism required to interpret perturbed  $\gamma$ – $\gamma$  directional correlations measured with a multidetector array following a nuclear reaction was described. The formalism was applied to design magnetic moment measurements which employ the Australian National University Compton-suppressed germanium-detector array CAESAR. In this paper, the experimental technique is described along with technical aspects of the data analysis, and the measurements are discussed in the context of related types of magnetic moment

measurements. The abbreviation PDCO will be used to designate Perturbed  $\gamma$ – $\gamma$  Directional Correlations from reaction-Oriented nuclei, and Ref. [1] will be referred to as Paper I.

In Section 2, the experimental techniques for measuring the  $g$  factors of short-lived excited states in nuclei are reviewed with an emphasis on measurements in neutron-deficient nuclei. The present experimental technique is then described. Experimental details of some of our first PDCO measurements are outlined in Section 3. The following section aims to give further insight into the technique by discussing details of the reaction kinematics, hyperfine fields and expected precessions for one of the measurements. It also reviews some of the concepts of PDCOs from an intuitive perspective. The analysis procedures developed for extracting the  $g$  factor from a measured perturbed

\*Corresponding author. Tel.: +61-2-6125-2097; fax: +61-2-6125-0748.

E-mail address: andrew.stuchbery@anu.edu.au (A.E. Stuchbery).

directional correlation are described in Section 5. A selection of experimental results is presented in Section 6, after which follows a summary and concluding comments.

As the initial aim of the experimental program was to employ perturbed directional correlations following heavy-ion induced reactions to measure the  $g$  factors of sub-nanosecond states in neutron-deficient nuclei, the focus here is upon magnetic interactions and the extraction of  $g$  factors. In certain cases, however, our measurements can give information on nuclear electric quadrupole moments. This aspect will be considered elsewhere [2]. Some aspects of the present work have been presented in conference papers (e.g. [3]).

## 2. Experimental principles and requirements

The measurement of  $g$  factors for short-lived states in neutron-deficient nuclei, particularly those with  $A \gtrsim 100$ , presents an experimental challenge for several reasons. The short lifetimes of the states require that the nuclei of interest be subjected to an intense magnetic field and, in practical terms, this usually means that the excited nuclei must be recoil-implanted into a suitable ferromagnetic host so that they experience intense hyperfine magnetic fields. While the recoiling ions are in motion, they experience the *transient* field [4]; then, after the ions come to rest, they experience the *static* field [5–8]. When the response of the nucleus to such fields after ion implantation is measured via the perturbations of the angular correlations (or distributions) of  $\gamma$ -ray radiation emitted from the excited nuclei, the technique is usually referred to as the IMplantation Perturbed Angular Correlation/Distribution (IMPAC/IMPAD) technique, [4,9,10].

### 2.1. Transient fields

The ‘thin-foil’ transient-field technique, in which the moving ions traverse a ferromagnetic foil and then come to rest in a non-magnetic medium, has been used extensively to measure the relative  $g$  factors of low-spin states in stable nuclei following Coulomb excitation [4,11–21]. Conventionally, the

nuclei of interest are contained in the first layer of a multilayer target [4], but recently projectile-excitation measurements, in which the beam species is the isotope of interest, have been developed and exploited [22–27]. In future, projectile-excitation measurements on rare-isotope (radioactive) beam species will become feasible. At present, however, neutron-deficient nuclei are most readily created and excited in heavy-ion fusion–evaporation reactions. Unfortunately, for most heavy nuclei so created, there is a delay of the order of a few picoseconds between the formation of the nucleus and its subsequent decay into the intensely populated, discretely observed states at low to medium spins. In a standard type of transient-field measurement, therefore, the recoiling nuclei will have come to rest and the transient field will have ceased to act by the time the discrete states are populated. Consequently, the transient-field technique has been used following (HI,xn) reactions primarily to measure the average  $g$  factors of the continuum of high-spin states above the yrast line [28–36]. We will describe a PDCO measurement of this type in Section 6.1. There have been a few measurements in which a vacuum gap is introduced between the ‘target’ foil and the ferromagnetic layer of the multilayer target to delay the transient-field effect so that selected discrete states are perturbed [37–41]; however these measurements are difficult and the statistical precision of the results can be low. (See Ref. [3] for further discussion.) When such measurements employ  $\gamma$ – $\gamma$  coincidences, the formalism of perturbed DCOs should be used to analyze the data.

### 2.2. Static fields

In the ‘thick-foil’ or static-field type of IMPAC measurement, which is the original IMPAC technique [9], the implanted nuclei stop in the ferromagnetic medium. This technique was widely used from the late 1960s until the mid-1970s to measure  $g$  factors of low-excitation states in stable nuclei following Coulomb excitation. After it was discovered that the transient field increases with the velocity of the moving ion, the static-field technique was largely abandoned in favor of the transient-field technique, at least for studies on the

stable nuclides. Compared with the transient-field technique, the static-field technique has the disadvantages that (i) the level lifetimes must be known accurately, and (ii) corrections must be made for the transient-field contribution to the total observed precession of the implanted nucleus. On the other hand, the static-field IMPAD technique has continued to find use in the study of selected unstable nuclei populated following heavy-ion induced reactions [42–45]. We will describe PDCO measurements using static fields in Section 6.2.

### 2.3. Beam induced reactions on the host

Once one moves away from Coulomb excitation, i.e. employs reactions where the beam energy is above the Coulomb barrier on the target material, it becomes likely that the beam will also be above the Coulomb barrier on the ferromagnetic host. In fact, this becomes a major limitation on the application of in-beam IMPAC/D measurements to heavy nuclei: in many cases the background radiation from the beam-induced reactions on the ferromagnetic host can greatly exceed the radiation from the excited nuclei of interest. This problem can be overcome or avoided in particular cases, e.g. by employing an implantation-decay version of the IMPAC technique as described in Ref. [46], by using inverse reactions [29–31], or by using a ferromagnetic host material that also serves as the target [28]. Coincidence measurements like those described below also help to overcome this problem since coincidence spectra are much ‘cleaner’ than singles spectra.

### 2.4. Fission fragments

The focus here is on accelerator-based measurements following heavy-ion induced reactions which tend to populate neutron-deficient nuclei. Measurements on fission fragments can be applied to study neutron-rich nuclei [47–49]. The  $g$  factors of low-excitation states in neutron-rich nuclei, populated by the  $\beta$  decay of fission fragments after on-line isotope separation, have been measured in several cases, e.g. Refs. [47,48]. Recently, Smith et al. [49] have shown that the  $g$  factors of excited states in

fragments from a  $^{252}\text{Cf}$  source can be measured by means of perturbed angular correlations in a multidetector array. The formalism of conventional angular correlations (with no alignment in the initial state) is sufficient to analyze these measurements and we will not consider them further here.

### 2.5. $g$ factors from perturbed DCOs

The PDCO technique in the form we have developed it to date is essentially the conventional static-field implantation type of IMPAC or IMPAD measurement [9,10], but employing a multidetector array to observe perturbed  $\gamma$ – $\gamma$  correlations from aligned states that have been populated following heavy-ion induced reactions. Previous, more conventional, measurements have usually observed perturbed angular distributions following such reactions or  $\gamma$ – $\gamma$  angular correlations from states with no initial alignment. As is evident from Paper I, the formalism becomes more complex in the case of perturbed DCOs, but there are several advantages:

- the coincidence spectra give better signal-to-noise than singles spectra, ameliorating the problem associated with background radiation from the ferromagnetic host;
- the execution of the experiments is relatively straight forward;
- the observables of interest are overdetermined and there are many internal consistency-checks in the data;
- the precession of an individual state of interest can be separated from the precessions of the states that feed it;
- states with lifetimes between a few tens of picoseconds and a few nanoseconds, in a wide range of nuclei, can be studied.

We will elaborate on these points in the following. Fig. 1 illustrates the improvement in peak-to-background obtained in coincidence spectra over singles measurements.

Our primary interest, at least in the first place, was to measure the  $g$  factors of low-spin states with lifetimes in the range between about 50 ps and a few nanoseconds. However, information on the high-spin states that experience the transient

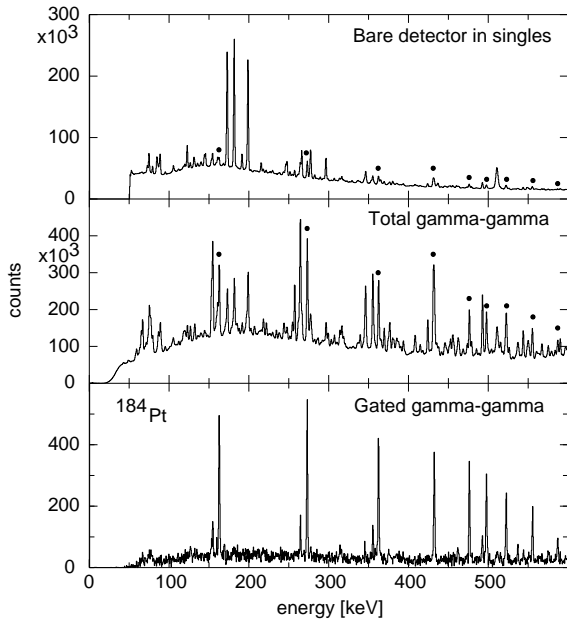


Fig. 1. Examples of singles and coincidence  $\gamma$ -ray spectra observed following 145 MeV  $^{29}\text{Si}$  induced reactions on  $^{\text{nat}}\text{Gd}$ . The upper panel shows a singles spectrum obtained with a bare Ge detector, the middle panel shows the projection of the total  $\gamma$ - $\gamma$  matrix observed with the CAESAR array of seven Compton suppressed Ge detectors, and the lower panel shows a sum of coincidence gates on transitions in the ground-state band of  $^{184}\text{Pt}$ . More stringent coincidence requirements reduce the number of counts in the spectrum but improve the peak-to-background significantly.

field while the nuclei are in motion immediately following the reaction is automatically included in the data set, as is information on the static-field precessions of any longer-lived high-spin states (i.e. nanosecond isomers). The PDCO technique complements and extends existing techniques. For example, the implantation-decay technique [46] can be used to connect  $g$  factor measurements in stable isotopes with those in unstable nuclei in a systematic fashion, forming a bridge between PDCO measurements in neutron-deficient nuclei and the well-studied stable nuclides.

### 3. Experimental procedures and apparatus

In a first measurement,  $^{81}\text{Sr}$  and neighboring nuclei were populated following 95 MeV  $^{28}\text{Si}$

induced reactions on a thick natural Fe target that also served as the ferromagnetic host. In a second case, the neutron-deficient platinum isotopes between  $^{180}\text{Pt}$  and  $^{184}\text{Pt}$  were populated simultaneously by 145 MeV  $^{29}\text{Si}$  induced reactions on natural Gd (again both the target and the ferromagnetic host). The magnetic moments of the  $2_1^+$  states in  $^{180}\text{Pt}$  and  $^{184}\text{Pt}$  have been measured by the implantation-decay technique [46,50], which provides a benchmark for the new technique. In the new data we have simultaneous, relative measurements for states in  $^{180,182,184}\text{Pt}$ .

The Australian National University array CAESAR [51], configured with seven Compton suppressed Ge detectors, all in the same plane as the beam, was used. The detector angles are summarized in Table 1 and further details of the array are given in Paper I. A compact electromagnet was designed and built [52] to fit in CAESAR, as is indicated schematically in Fig. 2. The field direction is perpendicular to the plane of the detectors. Technical drawings of the electromagnet and target chamber are presented in Figs. 3 and 4. The field produced at the target location as a function of the magnet current is shown in Fig. 5. Note that the target plane is at  $65^\circ$  to the beam.

Since the magnet coils are located inside the vacuum chamber they are encapsulated and

Table 1  
Detector numbering and angles in the CAESAR array

Number	$\vartheta^\circ$	$\varphi^\circ$	$\theta$
1	144.5	0	+144.5
4	146.0	180	−146.0
2	96.5	0	+96.5
5	98.0	180	−98.0
3	48.0	0	+48.0
6	49.5	180	−49.5
7	0.0	0	0

The angles  $\vartheta$  and  $\varphi$  are in spherical polar coordinates with the  $z$ -axis along the beam and the  $x$ -axis (i.e.  $\varphi = 0$ ) vertically upwards. The equivalent angles in the detector plane, where the beam axis is  $\theta = 0$  and  $-180^\circ \leq \theta \leq 180^\circ$ , are shown in the last column. The detectors are grouped in pairs that are placed symmetrically about the beam axis. See also Fig. 2.

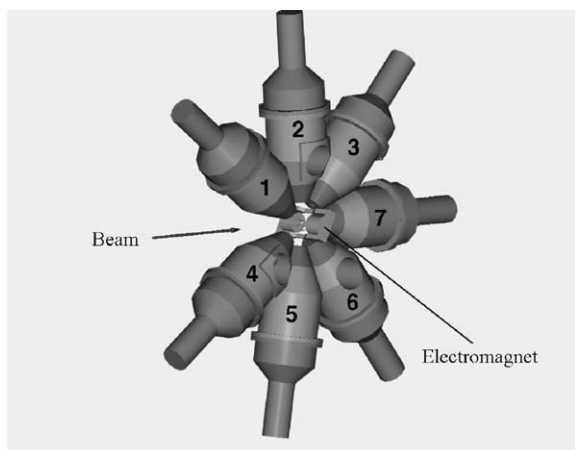


Fig. 2. Diagram showing the CAESAR array and the location of the electromagnet within it. The return yokes are at  $65^\circ$  and  $245^\circ$  with respect to the beam so as to avoid shadowing the  $\gamma$ -ray detectors.

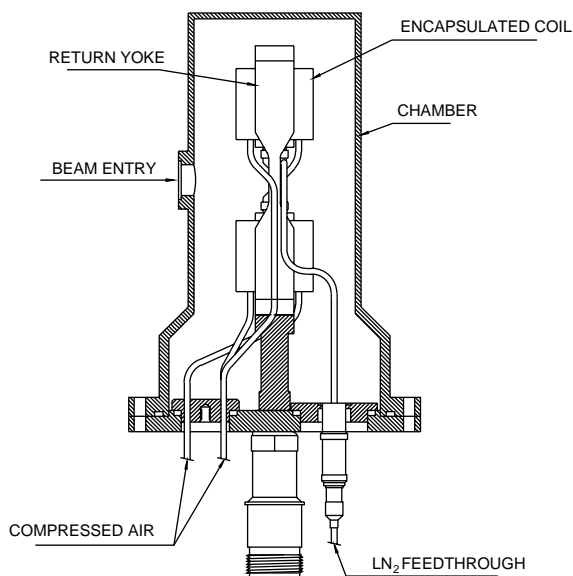


Fig. 3. Electromagnet and target chamber for use in the CAESAR array. Side view. See also Fig. 4.

provision is made for cooling them by flowing compressed air through the encapsulated volume. The target frame is thermally insulated from the poles of the magnet and may be cooled to about  $-180^\circ\text{C}$  by flowing cold nitrogen gas. The target

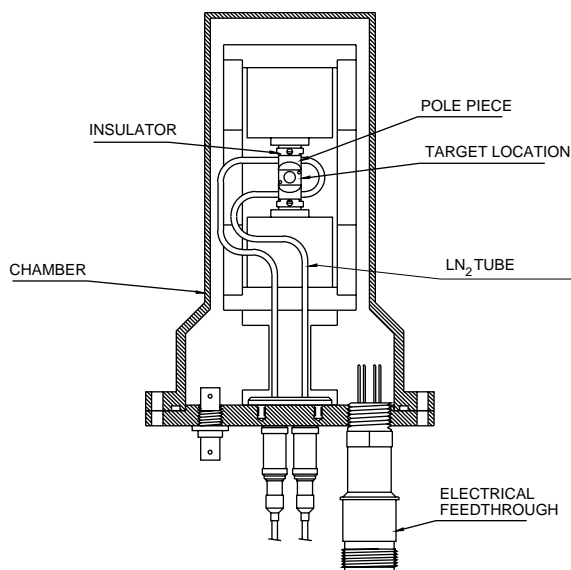


Fig. 4. Electromagnet and target chamber for use in the CAESAR array. View perpendicular to the target plane from the beam side. See also Fig. 3.

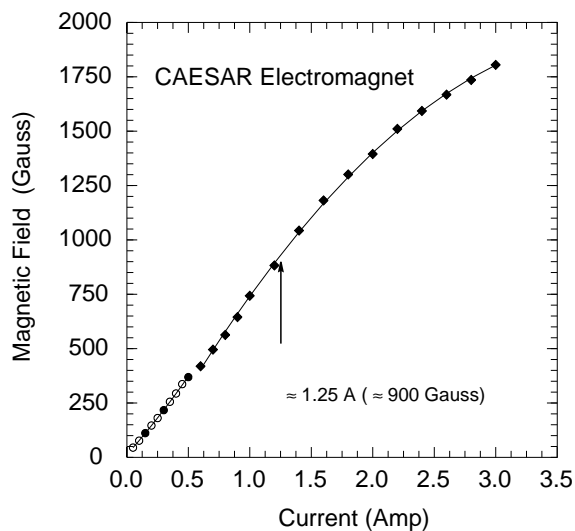


Fig. 5. Magnetic field versus current for the magnet in Figs. 3 and 4. The current is as read off the power supply which has 0.5 A (circles) and 5 A (squares) meter ranges.

temperature is monitored by a diode attached to the target mount.

An external field of 0.08 T was used to polarize the Fe hosts, while the experiments with Gd hosts

were performed with an applied field of 0.09 T. The field direction was reversed automatically approximately every 15 min. We define the positive field direction (sometimes called ‘up’ and denoted by an upward arrow ‘ $\uparrow$ ’) to mean the field points toward the right when viewed from the beam direction, i.e. to the right of the detector plane in Fig. 2.

Data corresponding to the  $\gamma$ -ray energies and relative times, together with a field-direction tag, were written to disk, event-by-event, for subsequent off-line analysis.

#### 4. Reaction kinematics, hyperfine fields, PDCO principles

Before discussing the analysis of the data it is helpful to have an overview of the reaction kinematics and the hyperfine fields experienced by the implanted nuclei so that the magnitudes of the nuclear precessions can be estimated. These aspects are discussed in Section 4.1 using the case of  $^{184}\text{Pt}$  as an example. Section 4.2 reviews some of the results from Paper I to give an intuitive, physical motivation for the key features of typical perturbed directional correlations to be measured and interpreted in the PDCO technique.

##### 4.1. Cross-sections, kinematics and hyperfine fields

Fig. 6 shows statistical model [53] calculations of the cross-sections for  $^{29}\text{Si}$  induced reactions on the isotopes  $^{156,158,160}\text{Gd}$ . The  $^{\text{nat}}\text{Gd}$  target used in the experiments was effectively  $6.6 \text{ mg/cm}^2$  thick along the beam axis, so these cross-sections are sampled between the beam energy of 145 MeV and the Coulomb barrier,  $\sim 127 \text{ MeV}$ . It can be seen that the isotopes  $^{182}\text{Pt}$  and  $^{184}\text{Pt}$  are produced prolifically and cleanly, while the cross-section for  $^{180}\text{Pt}$  is somewhat smaller. These features are confirmed experimentally in  $\gamma$ -ray spectra like those shown in the upper and middle panels of Fig. 1.

The calculations for the  $^{29}\text{Si}$  beam on  $^{56}\text{Fe}$  were included in Fig. 6 to demonstrate the advantage of using Gd as the ferromagnetic host rather than Fe. If the Pt nuclei were produced in a thin Gd layer

and recoil-implanted into a layer of Fe immediately behind the Gd, the  $^{29}\text{Si}$  beam energy would be much higher than the Coulomb barrier for  $^{29}\text{Si}$  on  $^{56}\text{Fe}$ . Clearly, there would be a large total-fusion cross-section for  $^{29}\text{Si}$  on the Fe host, which would be fragmented into very many reaction channels and cause a large increase in the  $\gamma$ -ray background level.

Details of the reaction kinematics at representative steps through the target are given for the example of  $^{184}\text{Pt}$  in Table 2. The reactions take place primarily in the front  $2 \text{ mg/cm}^2$  of the target and the beam approaches the Coulomb barrier after traversing  $\sim 3 \text{ mg/cm}^2$  of Gd. The energies with which the Pt nuclei recoil are very similar, whether the interaction takes place at the front of the target or at some depth. As a consequence, the recoils all have a similar range, all stop well within the Gd layer, and all experience a similar net transient-field interaction,  $\phi$ , where

$$\phi = -(\mu_{\text{N}}/\hbar) \int_0^{t_s} B_{\text{tr}}(t) dt. \quad (1)$$

In this expression  $\mu_{\text{N}}$  is the nuclear magneton,  $t_s$  is the time taken for the recoiling evaporation residues to stop in the Gd target, and  $B_{\text{tr}}(t)$  is the transient-field strength, which varies with time as the nuclei slow down. The Rutgers parametrization [55] of the transient field was used to evaluate the  $\phi$  values in Table 2.

It is now helpful to estimate the magnitudes of the precessions due to transient and static fields accumulated by states below  $I^\pi = 14^+$  in the ground-state band of  $^{184}\text{Pt}$ . Since the reaction populates highly-excited states at an average entry spin of around  $36\hbar$ , the net precession of the ground-band states has a component due to feeding from higher states populated in the reaction along with the precession that takes place in the state itself. ( $I^\pi = 14^+$  is chosen for this exercise because it turns out to be the highest state for which the feeding precession can be measured in the present experiment.)

Fig. 7 is a schematic representation of the hyperfine fields experienced by recoiling platinum nuclei as they slow and stop in the Gd target following  $^{29}\text{Si}$  induced reactions at 145 MeV. The transient field acts only while the Pt nuclei are in

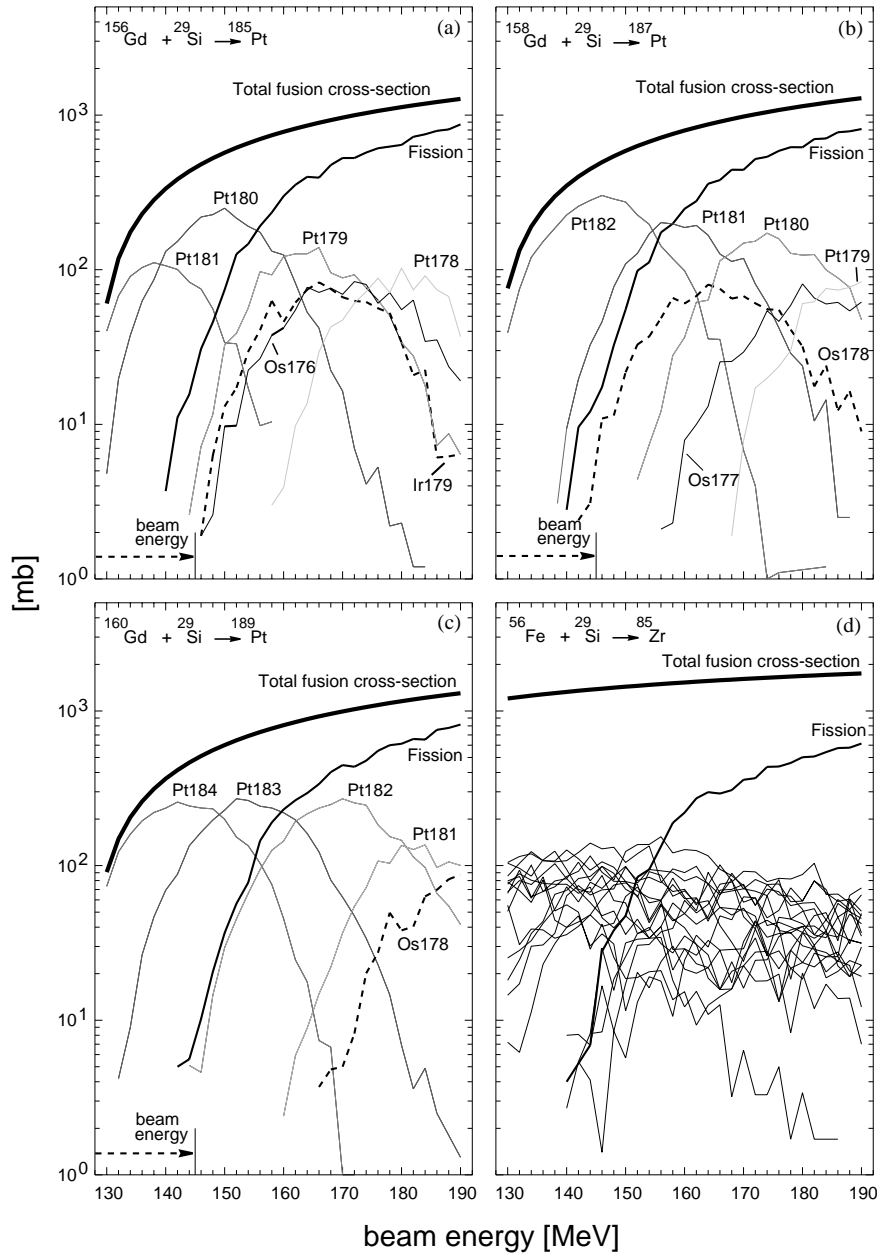


Fig. 6. Calculated cross-sections: (a–c)  $^{156,158,160}\text{Gd} + ^{29}\text{Si}$  and (d)  $^{56}\text{Fe} + ^{29}\text{Si}$ .

motion and decreases rapidly to zero as the recoiling nuclei come to rest within 2 ps of the nuclear reaction. Then follows a period of the order of a few picoseconds in which the violent collision cascades and thermal motion associated with the stopping process quench the static

hyperfine field [56–59]. The static field [60] begins to act on the implanted Pt nuclei once the implanted ion and the host reach equilibrium. It will become apparent in the following discussion that the period during which the static field is quenched can be ignored in the present  $g$  factor

Table 2

Reaction kinematics for  $^{184}\text{Pt}$  following the  $^{29}\text{Si}+^{160}\text{Gd}$  reaction

$x_{\text{tgt}}$ (mg/cm <sup>2</sup> )	$E_{\text{Si}}$ (MeV)	$\sigma$ (mb)	$E_{\text{Pt}}$ (MeV)	$R$ (mg/cm <sup>2</sup> )	$t_s$ (ps)	$\phi$ (mrad)
0	145	234	22.2	2.63	1.78	−139
1	140	229	21.5	2.56	1.75	−136
2	135	176	20.7	2.48	1.71	−133
3	130	68	19.9	2.40	1.69	−130

$x_{\text{tgt}}$  specifies the depth within the target at which the reaction takes place.  $E_{\text{Si}}$  is the energy of the beam at that point and  $\sigma$  is the cross-section for the production of  $^{184}\text{Pt}$  at that energy.  $E_{\text{Pt}}$  is the energy with which the resultant Pt nuclei recoil,  $R$  is their range and  $t_s$  is the stopping time.  $\phi$  is an estimate of the transient-field precession for a unit  $g$  factor. These calculations use the stopping powers of Ref. [54].

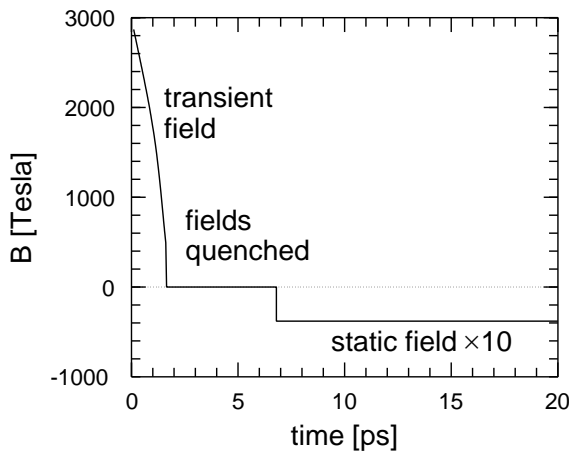


Fig. 7. Hyperfine fields experienced as a function of time by recoiling Pt nuclei after 145 MeV  $^{29}\text{Si}$  induced reactions on  $^{\text{nat}}\text{Gd}$ . The transient field and static fields have been measured for Pt in Gd (see, e.g. Refs. [19,60]). As the quenching time due to pre-equilibrium effects associated with the implantation process [56–59] has not yet been studied in Gd hosts, that shown is the time measured under similar conditions for Fe hosts [59].

measurements, although in other cases it might be more critical.

The absence of Doppler shifts in the  $\gamma$ -ray spectra (e.g. lower panel of Fig. 1) makes it evident that the recoiling nuclei have all stopped in the Gd host by the time the ground-band states with  $I \leq 14$  are populated. This is consistent with the lifetime measurements of Garg et al. [61], using the  $^{154}\text{Sm}(^{34}\text{S}, 4n)^{184}\text{Pt}$  reaction at 160 MeV, which suggest that the  $14^+ - 18^+$  states are populated around 2 ps after that reaction.

Assuming that the ground-band ‘probe’-states below  $I = 14$  inherit the same ‘quasicontinuum’ feeding precession due to the transient-field interaction, as has been found in previous studies (e.g. Ref. [36]), and that the average high-spin  $g$  factor is  $\langle g \rangle \sim 0.4$ , we estimate  $\Delta\theta_{\text{feed}} = \langle g \rangle \phi = -54$  mrad. (This in fact is very close to the experimental value.)

The static-field precessions of a state with lifetime  $\tau$  is given by

$$\omega\tau = -g(\mu_N/\hbar)B_{\text{st}}\tau \quad (2)$$

where the static-field strength  $B_{\text{st}}$  for Pt in Gd can be taken as  $-38$  T [60]. The lifetimes in  $^{184}\text{Pt}$  have been measured [61,62]. Table 3 gives estimates of the precessions of the individual states along with estimates of the total static-field precession accumulated in the cascade starting from the  $14^+$  state, assuming that the ground-band states all have  $g \sim 0.3$ , similar to the experimental value for the  $2^+$  state [46].

It can be seen from Table 3 that, with the exception of the  $2^+$  state, the precession angles (both transient and static) are small ( $\lesssim 100$  mrad). This is important because in such cases the magnetic perturbations can be treated as simple rotations of the correlation pattern about the field direction with negligible attenuation of the anisotropy. It follows that the observed net precession in any kind of perturbed angular-correlation measurement can be analyzed in terms of a sum over the precessions of the contributing components. Only for the longer-lived  $2^+$  state is there a large precession angle that gives rise to both a



Table 3

Estimates of precessions in the ground-state band of  $^{184}\text{Pt}$ 

Level	$\tau^a$ (ps)	$\omega\tau^b$ (mrad)	$\sum \omega\tau_{\text{casc}}^c$ (mrad)	$\Delta\theta_{\text{feed}} + \sum \omega\tau_{\text{casc}}^d$ (mrad)	$Q_I^e$	$Q_{\text{casc}}^f$
$14^+$	2.0	1.1	1.1	−53	0.22	0.22
$12^+$	2.3	1.3	2.4	−52	0.27	0.65
$10^+$	1.7	0.9	3.3	−51	0.17	1.0
$8^+$	3.1	1.7	5.0	−49	0.52	1.0
$6^+$	8.8	4.8	9.8	−44	0.71	1.0
$4^+$	36.5	19.9	29.7	−24	0.94	1.0
$2^+$	543	296.5	326.2	+272	0.99	1.0

<sup>a</sup> Mean lifetimes from Ref. [61], except for the  $2^+$  state which is an average of Refs. [61,62].<sup>b</sup> Static-field precession of designated state.<sup>c</sup> Cumulative static-field precession in the cascade decaying from the  $14^+$  state.<sup>d</sup> Net precession for the cascade below the  $14^+$  state.<sup>e</sup> Estimated factor by which the static-field precession of the state would be quenched if populated by fast (2 ps) sidefeeding.<sup>f</sup> Estimated factor by which the static-field precession of the state would be quenched if populated via the cascade below the  $14^+$  state.

rotation and attenuation of the angular correlation pattern.

For the  $6^+$  and higher states, the transient-field precession inherited from the quasicontinuum feeding dominates over the static-field contributions, which are small, if not negligible. The transient- and static-field precessions are of similar magnitude for the  $4^+$  states; and in the  $2^+$  states, the effect of the transient field in the feeding process is a small correction to the larger static-field precession.

These features, coupled with the ability to select particular transitions for the  $\gamma$ – $\gamma$  coincidence requirement in the PDCO technique, make the separate extraction of the high-spin transient-field precessions and the low-spin static-field precessions reliable and relatively straightforward.

Estimates of the factor by which the static-field precessions would be quenched by pre-equilibrium effects associated with the implantation process [56–59] are included in Table 3. The quantity  $Q_I$  is the quenching factor that would apply if the state I were populated by side-feeding about 2 ps after the reaction, while  $Q_{\text{casc}}$  is the factor that would apply when the state I is populated in cascade following the decay of the  $14^+$  state. Clearly, these factors differ significantly from unity only when the static-field precession is already very small. It is useful to keep in mind that a quenched-field pre-equilibrium interval separates the transient and

static field regimes, but its effect is so small in the present work that it can be ignored when analyzing the data. It might become significant in reactions which populate the states of interest more directly, and when the static field gives rise to larger precessions ( $> 10$  mrad) for states with lifetimes of a few picoseconds.

#### 4.2. PDCO concepts

The PDCO formalism was presented rigorously in Paper I. However, since the formalism is not very transparent, some of the concepts will be reviewed here in a more qualitative and intuitive way.

When two  $\gamma$  rays are observed in coincidence following the formation of a partially aligned high-spin state, the observed correlations have some of the features of a conventional  $\gamma$ – $\gamma$  angular correlation from an initial state with no alignment, and some of the features of a  $\gamma$ -ray angular distribution with respect to the beam axis, but they differ from both. In the cases of present interest the initial high-spin state has its spin rather well aligned in the plane perpendicular to the beam direction, so we begin by taking ordinary angular distributions as a point of reference.

Fig. 8, reproduced from Paper I, shows the calculated unperturbed and perturbed DCOs for a  $4^+ \rightarrow 2^+ \rightarrow 0^+$  cascade observed with the CAESAR

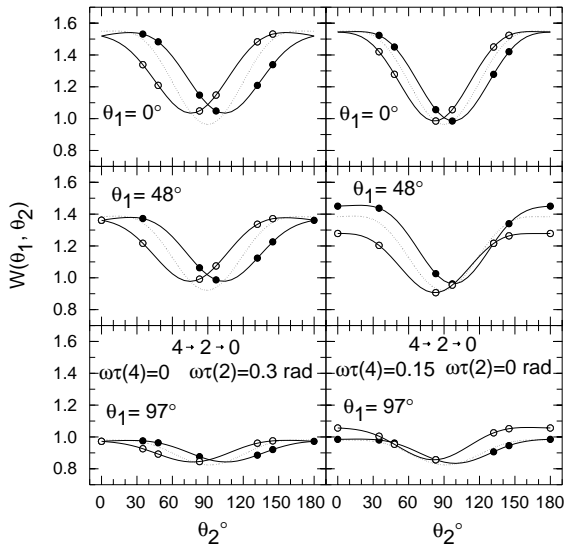


Fig. 8. Calculated unperturbed (dotted) and perturbed (solid) DCOs for a  $4^+ \rightarrow 2^+ \rightarrow 0^+$  cascade observed with the CAESAR array. The left panels show a perturbation of the  $2^+$  state, while the right panels show a perturbation of the  $4^+$  state. The data points indicate the angles sampled by the array. Positive (negative) precession angles are denoted by solid (open) symbols. The case where  $\theta_1 = 145^\circ$ , which is intermediate between the  $0^\circ$  and  $48^\circ$  cases, is not shown. This figure is reproduced from Paper I.

array. This case is typical of any stretched E2 cascade. The  $4^+ \rightarrow 2^+$  transition is registered at angle  $\theta_1$  while the  $2^+ \rightarrow 0^+$  transition is detected at angle  $\theta_2$ . In the CAESAR array  $\phi_1$  and  $\phi_2$  are either  $0^\circ$  or  $180^\circ$ , and the detectors are located at approximately  $0^\circ, \pm 48^\circ, \pm 97^\circ$ , and  $\pm 145^\circ$  to the beam; hence the data for all two-detector combinations can be mapped onto four plots with  $\theta_1 = 0^\circ, 48^\circ, 97^\circ$  or  $145^\circ$  and  $0 \leq \theta_2 \leq 180^\circ$ .

As already noted, the alignment of the  $4^+$  state due to the reaction (and unobserved  $\gamma$ -ray decays above the  $4^+$  state) is centered in the plane perpendicular to the beam axis. It can be seen from the unperturbed DCOs in Fig. 8 that the intensity of the  $2^+ \rightarrow 0^+$  transition with respect to the beam direction is peaked near the beam axis and is smallest at  $90^\circ$  to the beam—roughly like that of a typical stretched E2 transition observed in an angular-distribution measurement. The difference comes about because the detection of the  $4^+ \rightarrow 2^+$  transition has modified the alignment

of the  $4^+$  state. As an intuitive approximation, the detection of a  $\gamma$  ray tends to align the state populated in such a way that its spin is in the plane perpendicular to the direction of detection. Most of the features of the unperturbed DCOs in Fig. 8 can be understood in terms of this mechanism. For example, when the  $4^+ \rightarrow 2^+$  transition is detected at  $\theta_1 = 0^\circ$ , the alignment of the  $2^+$  state is even more sharply centered in the plane perpendicular to the beam axis than that of the  $4^+$  state. Thus the anisotropy of the DCO in the upper panels of Fig. 8 is greater than that of an angular distribution with the same reaction-induced alignment. Taking another example, the reduced alignment and reduced total intensity in the lower panels of Fig. 8, where  $\theta_1 = 97^\circ$ , stems from the fact that the detection of the  $4^+ \rightarrow 2^+$  transition near  $90^\circ$  to the beam must align the  $2^+$  spin in a plane that is largely orthogonal to the existing alignment of the  $4^+$  state.

Some general aspects of magnetic perturbations can now be considered. The perturbation in the left-hand panels of Fig. 8 is due to a pure magnetic interaction in the  $2^+$  state alone with  $\omega\tau = \pm 0.3$  mrad; this precession is of the magnitude expected in the measurements on the Pt isotopes. The right-hand panels show the effect of a magnetic interaction in the  $4^+$  state alone with  $\omega\tau = \pm 0.15$  mrad, which for pedagogical purposes is an exaggerated effect compared with those expected in the measurements. The coincidence requirement eliminates side-feeding to the  $2^+$  state. While the perturbation of the intermediate ( $2^+$ ) state is manifested as a rotation of the radiation pattern combined with a small attenuation of the anisotropy, the perturbation of the upper ( $4^+$ ) state, when plotted in this way, is a more complex combination of rotation, attenuation and change in total intensity. It is clear that when  $\theta_1 \neq 0$ , the PDCOs are sensitive to the perturbation of the feeding state (e.g.  $4^+$ ) and the intermediate state (e.g.  $2^+$ ) in a different way.

There is a more intuitive way to understand these magnetic perturbations because they stem from rotations of the radiation pattern about the field direction: the precession of the  $4^+$  state behaves like an equal rotation of all detection angles in the array with respect to the beam

direction, whereas the precession of the  $2^+$  level is manifest as a change in the effective angle between the detectors that detect the two  $\gamma$ -rays. When presented this way, it is tempting to say that the feeding perturbation in a PDCO measurement is somewhat akin to that in a conventional perturbed angular distribution measurement, whereas the perturbation of the intermediate state is more like that in a conventional perturbed  $\gamma$ - $\gamma$  correlation measurement. But, while such analogies may be useful, they must be treated with caution; a rigorous analysis requires the proper DCO formalism. For example, in general neither the unperturbed nor the perturbed correlations shown in Fig. 8 can be written exactly in terms of the familiar sum of even- $k$  Legendre polynomials,  $P_k(\cos \theta_2)$ , which would apply in conventional measurements. For the CAESAR array it can be done exactly only when  $\theta_1 = 0$ .

## 5. Analysis of PDCO data

In this section, we describe the analysis of the experimental data and address several practical aspects of extracting a precession angle  $\omega\tau$  from the PDCO data. The key aspect of the analysis procedures we use is to fit the data from all two-detector combinations simultaneously, whether we are primarily interested in the perturbed or unperturbed DCOs. A computer program [63] has been written for this purpose. Some features of this code are outlined below in Section 5.6.

### 5.1. Sorting and data manipulation

The first step in the data analysis was to sort the  $\gamma$ - $\gamma$  data from the seven detectors into 42 prompt-coincidence matrices with one detector on the  $x$ -axis and another detector on the  $y$ -axis, and with a separate matrix for each field direction. We also formed a total symmetrized  $\gamma$ - $\gamma$  matrix and a set of 14 matrices with one selected detector on the  $x$ -axis and the other six on the  $y$ -axis, and again separate matrices for the two field directions. The analysis of the PDCO data used the 42 matrices for the individual  $\gamma$ - $\gamma$  detector pairs; the other matrices were used primarily for cross checking.

The volumes of the peaks of interest were determined by gating on a line of interest and then measuring the area in the relevant peaks in the projected spectrum. When applying the PDCO formalism it does not matter which detector is on which axis of the matrix, or which transition is gated and which has its area measured in the projected spectrum. What is important is the order of the transitions in the nuclear level scheme and the angles at which the  $\gamma$  rays are detected.

Since the detectors in the CAESAR array are all in one plane, the DCO and PDCO functions can be written as  $W(\theta_1, \theta_2)$ , where  $\theta_1$  denotes the angle at which the first (i.e. higher excitation)  $\gamma$  ray is detected and  $\theta_2$  denotes the angle at which the second (i.e. lower excitation)  $\gamma$  ray is detected. We have found it helpful, in the analysis and presentation of the data for a particular cascade, to arrange the data such that a  $\theta_1$  value is selected and the data for the corresponding six values of  $\theta_2$  are grouped with it. The DCOs calculated in Paper I and the experimental results presented below are displayed in this way.

If we consider a two-fold coincidence between  $\gamma$  rays with energies  $E_{\gamma_1}$  and  $E_{\gamma_2}$  recorded in detectors  $i$  and  $j$ , respectively, at detection angles  $\theta_i$  and  $\theta_j$ , then the observed coincidence intensity is

$$N_{ij} = N_0 \epsilon_i(E_{\gamma_1}) \epsilon_j(E_{\gamma_2}) W(\theta_i, \theta_j) \quad (3)$$

where  $W(\theta_i, \theta_j)$  is the DCO function and  $N_0$  is the overall normalization factor that depends on the reaction cross-section, the beam intensity, the counting time, and other effects like electronic dead-time. The coincidence  $\gamma$ -ray detection efficiencies are denoted  $\epsilon_i(E_{\gamma_1})$  and  $\epsilon_j(E_{\gamma_2})$ .

Once the peak areas have been obtained, the next task in data analysis is to determine the alignment parameter  $\sigma/I$  of the initial state, which determines its statistical tensor,  $B_k(I)$  [64], where

$$B_k(I) = \sqrt{2I+1} \sum_m (-)^{I+m} \langle I - m | m | k 0 \rangle P_m. \quad (4)$$

$P_m$  specifies the  $m$ -substate population distribution of the state  $I$  and is approximated by a Gaussian

distribution,

$$P_m = \frac{\exp(-m^2/2\sigma^2)}{\sum_{m'=-I}^I \exp(-m'^2/2\sigma^2)}. \quad (5)$$

(See Paper I for further details.)

Provided the precession angles are not too big, the unperturbed DCO can be obtained from the PDCO data by adding the data for the two field directions together. This procedure is applicable for most of the strongly-populated states in the nuclei we have studied to date (the  $2_1^+$  states in the Pt isotopes are an exception). Apart from the overall normalization factor,  $N_0$ , the only unknown parameter, in principle, is then  $\sigma/I$ . However, the observed  $\gamma$ -ray intensities must be corrected for the relative detector efficiencies in the array, and it is to this that we now turn our attention.

## 5.2. Efficiency calibration

The relative coincidence efficiencies of each individual detector in an array are often assumed to be the same as the ‘singles’ efficiencies measured with a radioactive source and with the detectors ‘self-gated’, however the efficiencies so measured may not always be applicable to ‘in-beam’ data. (See, for example, the discussion in Ref. [65].)

Initially, the efficiencies of the CAESAR array in self-gated singles were calibrated with a  $^{152}\text{Eu}$  source. The energy-dependence of the efficiency for each detector was fitted to the polynomial function

$$\ln \epsilon(E_\gamma) = \sum_{i=0}^5 a_i (\ln E_\gamma)^i \quad (6)$$

where  $\epsilon(E_\gamma)$  is the detector efficiency at  $\gamma$ -ray energy  $E_\gamma$  in MeV. The singles efficiencies for six of the seven detectors in CAESAR are displayed in Fig. 9. (Dotted lines.)

The coincidence efficiencies were also measured for the 244.7–121.8 and 411.1–344.3 keV,  $4^+ \rightarrow 2^+ \rightarrow 0^+$  cascades in  $^{152}\text{Sm}$  and  $^{152}\text{Gd}$ , respectively, populated in the decay of  $^{152}\text{Eu}$ . These data exposed some differences at low energy between the self-gated singles efficiency and the coincidence efficiency. The adopted coincidence efficiencies are

shown as the solid lines in Fig. 9. Fig. 10 shows the angular correlation data obtained for the 244.7–121.8 keV cascade in  $^{152}\text{Sm}$  fitted with the adopted coincidence efficiency calibration.

Upon examining the in-beam DCO data, it was apparent that for some of the detectors there is a difference between the in-beam efficiency and that obtained with a radioactive source. This is most likely related to changes in the Compton suppression efficiency in-beam. Thus the coincidence efficiency calibration determined with the source is not always reliable for analyzing precise DCO data (cf. Ref. [65]). Note that this problem did not occur in our earlier work with an out-of-beam implantation-decay technique [46,66].

Fortunately, the DCO function is overdetermined and the required efficiencies can often be determined from the DCO data, provided the full angular correlation (DCO) is fitted for all of the two-detector combinations simultaneously. More specifically, for the CAESAR array configured with seven detectors there are 42 detector pairs that record the  $E_{\gamma_1}$ – $E_{\gamma_2}$  coincidence, i.e. 42 values of  $N_{ij}$  (Eq. (3)). On the other hand there are only 14 different coincidence efficiencies,  $\epsilon_i(E_{\gamma_1})$ ,  $\epsilon_j(E_{\gamma_2})$ , involved. In general, for an array with  $n_d$  detectors there are  $n_d \times (n_d - 1)$  pairs for each  $\gamma$ – $\gamma$  coincidence and  $2 \times n_d$  coincidence efficiencies. Provided that the form of the correlation function is known with only one or two free parameters (e.g. for a sequence of stretched quadrupole transitions), some—or all—of the detector efficiencies can be treated as free parameters (up to a normalization factor) in a simultaneous fit to the  $n_d \times (n_d - 1)$  data points,  $N_{ij}$ .

The fitted relative efficiencies for the detectors can also be constrained by the fact that the DCO functions for a cascade of stretched E2 transitions below a selected E2 transition are the same (cf. Fig. 2).

Some examples of fits to DCO data taken in the study of  $^{81}\text{Sr}$  and neighboring nuclei are shown in Fig. 11. We found in this case that the fitted efficiencies were usually within about 5% of the efficiencies measured with the source, but that for one detector the difference was more than 10%. The fits determine the efficiencies rather accurately

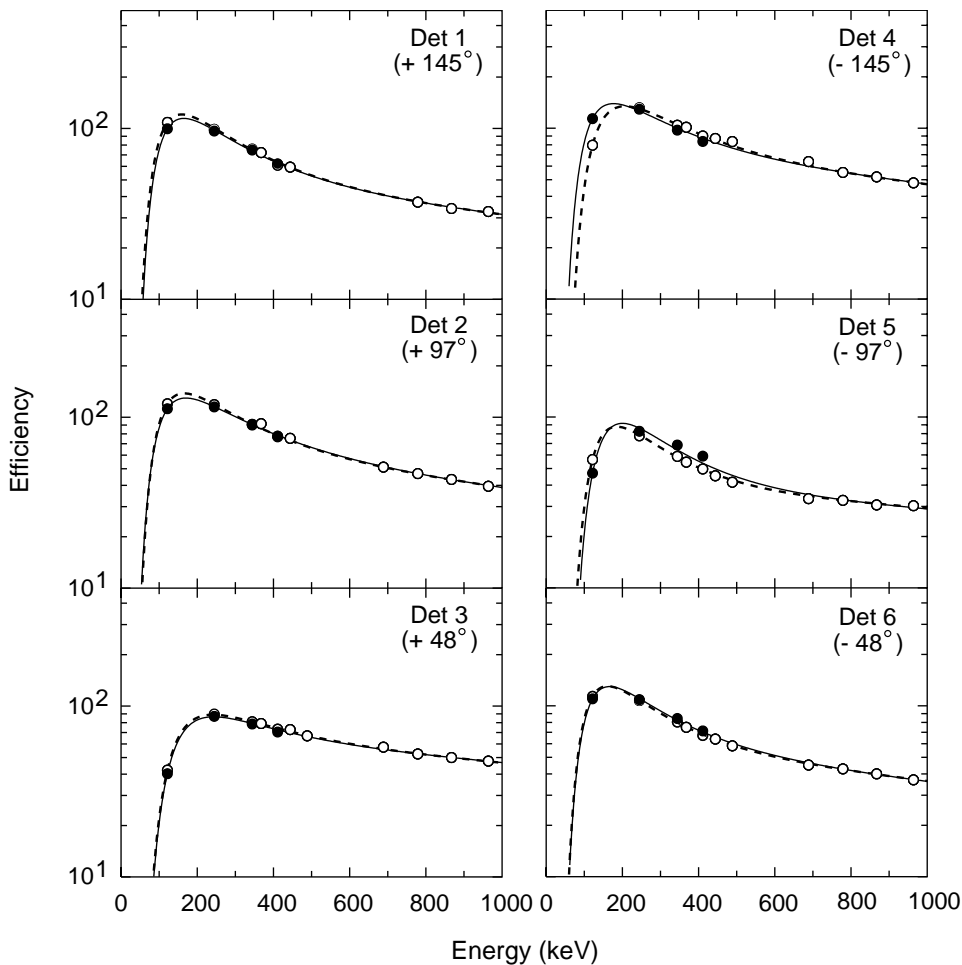


Fig. 9. Detector efficiencies determined with a  $^{152}\text{Eu}$  source. The dotted line shows the fit obtained for the self-gated singles measurement. The solid line shows a fit that takes into account the measurement of the coincidence efficiencies for the 245–122 keV and 411–344 keV cascades. In most cases the difference between the singles and the coincidence efficiency is small. Where present, any differences become more pronounced at low energy.

and are not strongly correlated with the alignment parameter. This can be attributed, in part, to the fact that the anisotropy is small when the first  $\gamma$  ray is detected near  $90^\circ$ —thus that subset of the data is more sensitive to the detector efficiencies than to the alignment of the initial state.

### 5.3. $\sigma/I$ from unperturbed DCOs

The value of  $\sigma/I$  (see Eqs. (4) and (5)) can be determined from fits to unperturbed DCO data such as those shown in Fig. 11. In many cases

there may be several measures of the alignment parameter for a state because the DCO function  $W(\theta_i, \theta_j)$  is identical for all transitions in a cascade of stretched E2 transitions below the first detected E2 transition. For example, as shown in Fig. 12, if the first detected radiation is the  $10^+ \rightarrow 8^+$  transition in  $^{184}\text{Pt}$ , then the unperturbed DCOs for coincidence with the  $8^+ \rightarrow 6^+$ ,  $6^+ \rightarrow 4^+$  or  $4^+ \rightarrow 2^+$  transition as the second detected radiation are the same within a normalization factor (related to the detection efficiencies) and each gives an independent measure of  $\sigma/I$  for the  $10^+$  state. For the  $6^+$

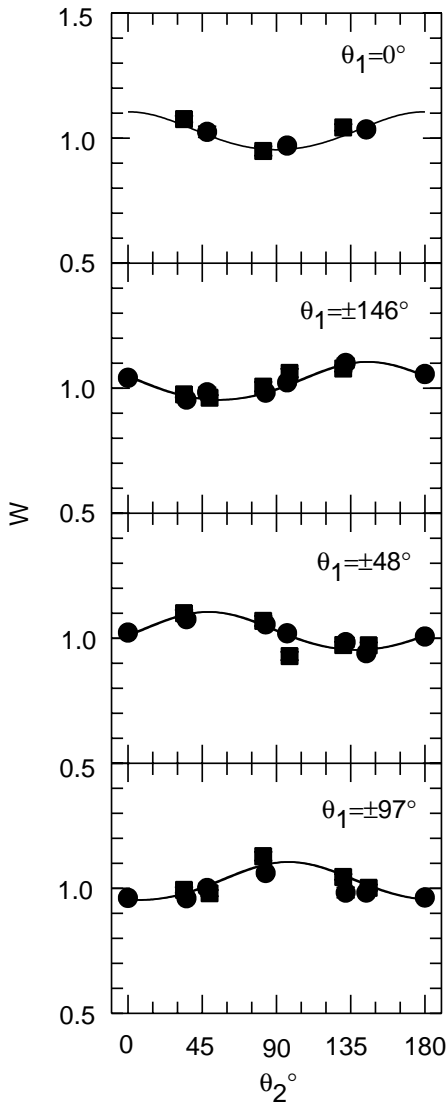


Fig. 10. Angular correlations measured for the 245–122 keV cascade in  $^{152}\text{Sm}$  populated in the decay of  $^{152}\text{Eu}$ . These angular correlation data were fitted with the PDCO formalism taking  $\sigma/I \rightarrow \infty$ . The data and fits are displayed in the same way that we present the DCO data, i.e. the 245 keV  $4^+ \rightarrow 2^+$  transition is detected at the specified angle  $\theta_1$  and the 122 keV  $2^+ \rightarrow 0^+$  transition is detected at angle  $\theta_2$ . Statistical errors are of the order of, or smaller than, the data symbols. (Circles are data from detectors 1–3 and 7, while squares represent data from detectors 4–6 in the CAESAR array.)

state and higher in  $^{184}\text{Pt}$ , the DCO data are well fitted with  $\sigma/I = 0.3$ , which agrees well with the value from angular distribution measurements

reported by Carpenter et al. [67] following the  $^{172}\text{Yb}(^{16}\text{O}, 4n)$  reaction at 91 MeV.

#### 5.4. $\sigma/I$ from angular distributions

The alignment parameter  $\sigma/I$  can also be determined from (singles) angular distribution measurements, since the angular distribution can be written as

$$W(\theta) = \sum_{k=0,2,4} a_k P_k(\cos \theta) \quad (7)$$

where

$$a_k = B_k(\sigma/I) F_k Q_k \quad (8)$$

and  $B_k$  is the statistical tensor (Eq. (4)),  $F_k$  is the  $F$ -coefficient, and  $Q_k$  is the solid-angle attenuation factor, as described in Paper I and the references therein. In Eq. (7)  $P_k$  is a Legendre polynomial and  $\theta$  is the angle of  $\gamma$ -ray detection with respect to the beam axis. Fig. 13 shows the  $a_k$  ( $k = 2, 4$ ) coefficients for stretched E2 transitions as a function of  $\sigma/I$  for  $Q_2 = Q_4 = 1$ . The shaded regions indicate the commonly reported measured  $a_k$  values and the range of  $\sigma/I$  values usually found for states populated following heavy-ion fusion–evaporation reactions.

The alignment parameters for  $^{78}\text{Kr}$  and  $^{81}\text{Sr}$  determined from the DCO data in Fig. 11 are  $\sigma/I = 0.36(2)$  for the states in  $^{81}\text{Sr}$  and  $\sigma/I = 0.45(2)$  for  $^{78}\text{Kr}$ . These values agree with the alignment parameters implied by the angular distribution measurements of Theisen et al. [68] for the  $^{56}\text{Fe} + ^{28}\text{Si}$  reaction at 88 MeV. Since  $^{81}\text{Sr}$  and  $^{78}\text{Kr}$  are populated by the  $2p_n$  and  $2p_\alpha$  channels, respectively, the reduced alignment for  $^{78}\text{Kr}$  can be associated with the emission of the  $\alpha$ -particle in that reaction channel.

An attempt was made to measure the alignment parameters for the Pt isotopes by performing angular distribution measurements with the same beam (145 MeV  $^{29}\text{Si}$ ) and target ( $^{155}\text{Gd}$ ) as used for the DCO measurements. For all but one or two transitions the alignment inferred from the singles measurement was much smaller than that obtained from the DCO data and was also in disagreement with the alignment observed in the angular distribution measurements for  $^{184}\text{Pt}$  reported by

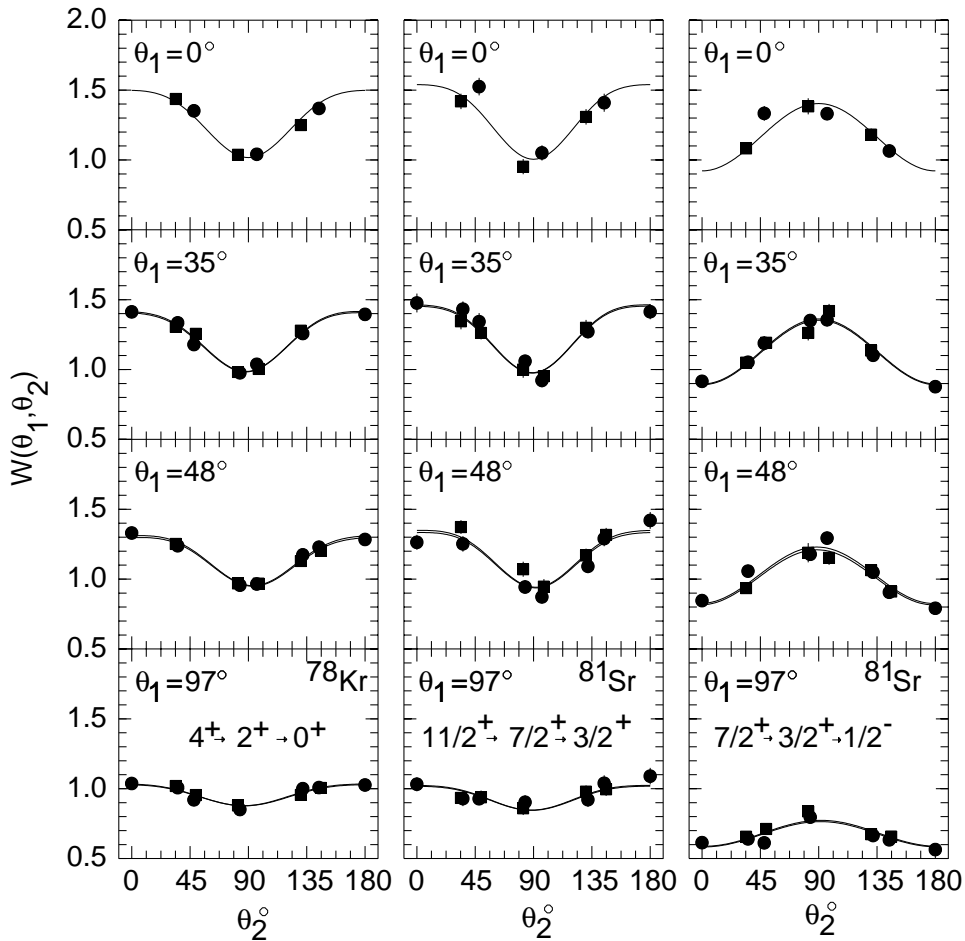


Fig. 11. Unperturbed DCOs in  $^{78}\text{Kr}$  and  $^{81}\text{Sr}$  obtained by adding the data for the two field directions. The detector efficiencies can be fitted along with the alignment parameter for the initial state. See text for further discussion.

Carpenter et al. [67]. At the same time, measurements on other nuclei made with the same apparatus resulted in angular distributions that agreed with previous, independent measurements. The discrepancy in our angular distribution measurements for the Pt isotopes stems mainly from the complexity of the singles spectrum obtained with the natural Gd target, which is shown in the upper panel of Fig. 1—nearly all of the lines of interest are contaminated.

Another contribution to the difference between the alignment observed in coincidence and in singles may be due to deorientation effects in high-spin isomers in  $^{182}\text{Pt}$  and  $^{184}\text{Pt}$  [67,69–71]

that eventually decay into the low-excitation states. This does not seem to be an important consideration in the present measurements, however, because little intensity in the low-spin yrast states stems from pathways that pass through the isomer.

Thus the alignment parameters can be determined either from angular distribution measurements or from unperturbed DCOs; however the chance of introducing systematic errors is minimized when the alignment parameters and the perturbations of the DCOs are measured under identical conditions, as we have done in the cases studied to date.

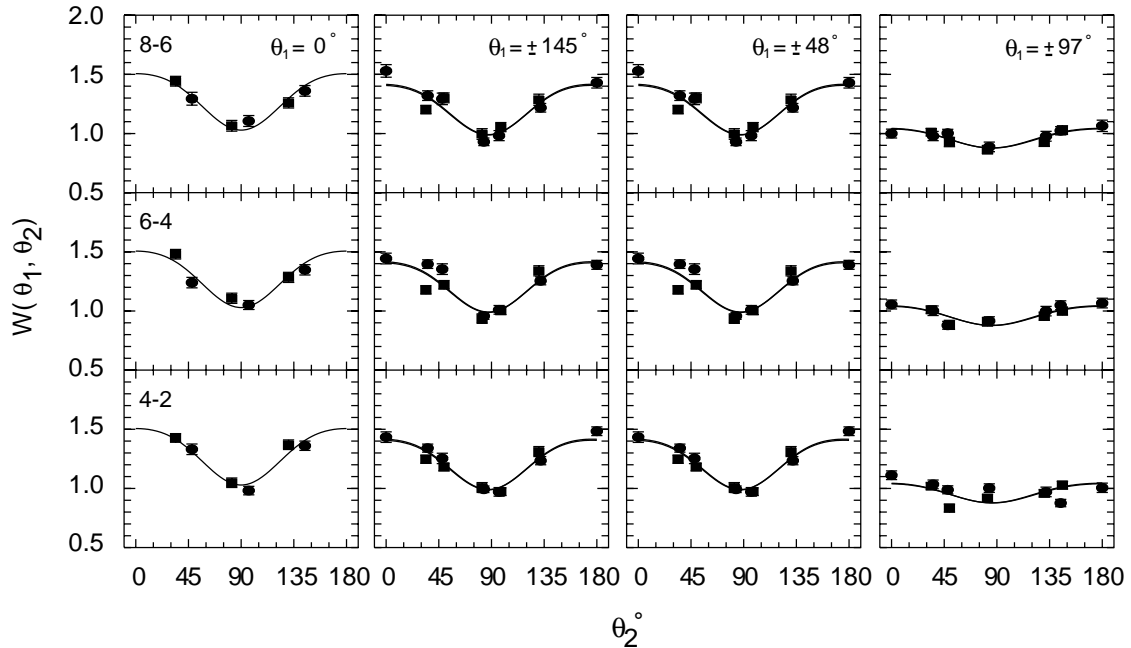


Fig. 12. DCO data for the ground-state band of  $^{184}\text{Pt}$ . In all cases the  $10^+ \rightarrow 8^+$  transition is detected: at  $0^\circ$  in the first column; at  $\pm 145^\circ$  in the second column; at  $\pm 48^\circ$  in the third column; and at  $\pm 97^\circ$  in the last column. The second transition detected is  $8^+ \rightarrow 6^+$  in the top row of panels,  $6^+ \rightarrow 4^+$  in the middle row, and  $4^+ \rightarrow 2^+$  in the bottom row. For a sequence of stretched E2 transitions, such as this, the fitted angular correlation in each column is the same.

### 5.5. Identification of perturbed states

Once  $\sigma/I$  has been determined, the precession angles can be extracted. Before discussing the determination of the precession from the PDCO data, we will outline a method we have found useful to identify which of the peaks in a complex spectrum show a significant perturbation. We apply this technique to the total projections of the  $\gamma$ - $\gamma$  data for each individual detector. Since these total projections are like multiplicity-gated singles spectra, the data can be evaluated approximately in terms of the formalism for perturbed angular distributions. This observation underpins the following procedure.

Differences between the data for the two field directions can be identified and displayed by constructing appropriate ‘sum’ and ‘difference’ spectra. In order to normalize the data for the two field directions such that the absence of a perturbation corresponds to a zero in the ‘difference’ spectrum, the total projections of the

coincidence data for a pair of detectors placed symmetrically about the beam axis are combined. For example, one such pair of detectors are those numbered 1 and 4 in Fig. 2 and Table 1, at  $+145^\circ$  and  $-146^\circ$ , respectively.

The spectra for the two detectors that are to be used must be gain-matched. Once this is done, double ratios [4] can be formed channel-by-channel, so that for each channel  $i$ ,

$$\rho_i = \sqrt{\frac{N_i(+\theta, +) N_i(-\theta, -)}{N_i(+\theta, -) N_i(-\theta, +)}} \quad (9)$$

and

$$\varepsilon_i = \frac{1 - \rho_i}{1 + \rho_i} \quad (10)$$

where  $N_i(\pm\theta, \pm)$  are the counts registered in channel  $i$  of the spectra from the two detectors at  $\pm\theta$ , for the two field directions. The statistical uncertainties  $\sigma_{\varepsilon_i}$  can also be evaluated channel-by-channel by standard procedures. The statistical significance (or weight) associated with  $\varepsilon_i$  is



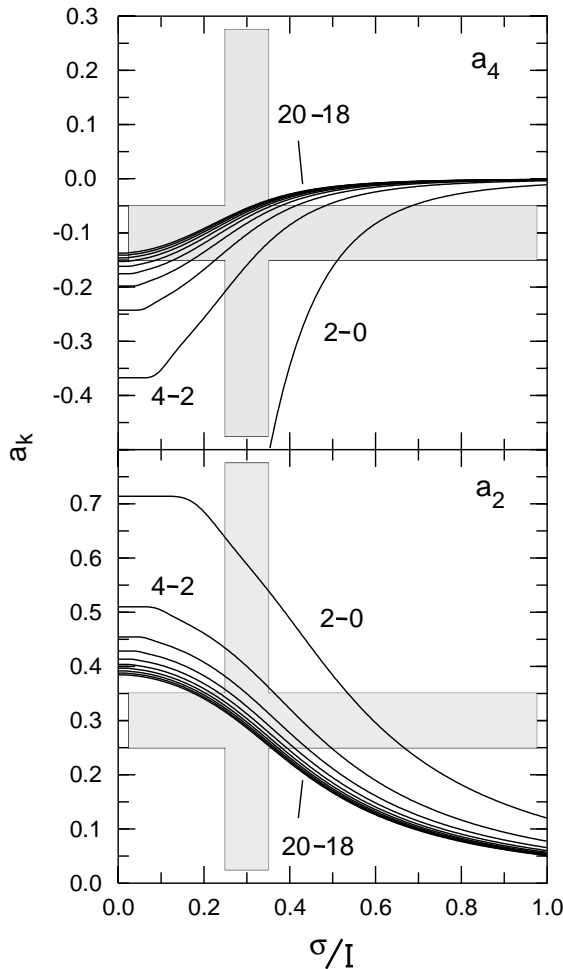


Fig. 13. Angular distribution coefficients for stretched E2 transitions as a function of the alignment parameter  $\sigma/I$ . The shaded regions indicate the commonly reported measured  $a_k$  values as well as the range of  $\sigma/I$  values usually found for states populated following heavy-ion fusion-evaporation reactions. The  $2^+$  and  $4^+$  states have significantly larger  $\sigma/I$  values than the high-spin states.

$w_i = 1/\sigma_{\epsilon_i}^2$ . Hence the  $\epsilon$  value for a peak is

$$\epsilon = \frac{\sum_i w_i \epsilon_i}{\sum_i w_i} \quad (11)$$

where the sum is now over the channels in the peak of interest.  $\epsilon$  can be obtained with standard peak fitting routines. Another way of looking at this is to recognize that the  $w_i$  spectrum is approximately

the logarithmic mean ‘sum’ spectrum since, for small precessions,

$$\begin{aligned} N_i(+\theta, +) &\approx N_i(+\theta, -) \approx N_i(-\theta, -) \\ &\approx N_i(-\theta, +) \approx \bar{N}_i \end{aligned}$$

and

$$\begin{aligned} w_i &\approx 16[N_i(+\theta, +)^{-1} + N_i(+\theta, -)^{-1} \\ &\quad + N_i(-\theta, -)^{-1} + N_i(-\theta, +)^{-1}]^{-1} \\ &\approx 4\bar{N}_i. \end{aligned} \quad (12)$$

Similarly, it can be shown that the weighted-epsilon spectrum,  $w_i \epsilon_i$ , is an average ‘difference’ spectrum. If  $\epsilon$  is small and the two detectors have somewhat different energy resolution it is difficult to get an accurate estimate of  $\epsilon$ . Thus this technique may not have general applications for extracting  $\epsilon$  quantitatively. It does, however, provide a very useful method for quickly identifying which lines in a complex spectrum show a significant perturbation. Examples of a ‘sum’ and a ‘difference’ spectrum, constructed from the total projections of the  $\gamma$ - $\gamma$  data for the detectors at  $\pm 48^\circ$  to the beam, following the  $^{nat}\text{Fe} + ^{28}\text{Si}$  reaction, are given in Fig. 14.

### 5.6. Fits to the correlations

A computer program has been developed to fit the PDCO data [63]. This program reads in the details of the detector array and all relevant information about the  $\gamma$ - $\gamma$  cascade, including the spins of the states and the multiplicities and mixing ratios of the transitions. The energy-dependent efficiency calibrations for each detector in the array are also specified, although these can also be varied in the fitting procedure, if applicable. The program also reads in the observed peak intensities for each  $\gamma$ - $\gamma$  coincidence of interest, which includes the data for each two-detector combination and for both field directions. The user can then select from several options to manipulate and fit the data.

In the first mode of operation the data for the two field directions are added together to give the ‘unperturbed’ DCO, as discussed in the first three subsections of the present section. In this mode Eq. (3) is fitted to the data, and hence the

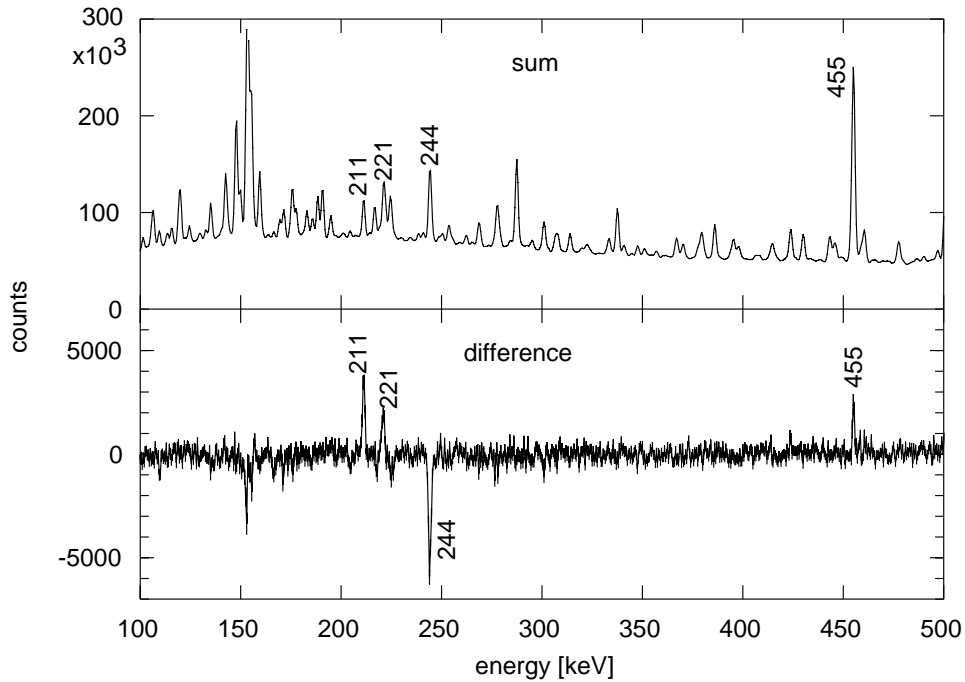


Fig. 14. Sum and difference spectra constructed from the total projections of the  $\gamma$ - $\gamma$  coincidence data for the detectors in CAESAR at  $\pm 48^\circ$  to the beam following 95 MeV  $^{28}\text{Si}$  induced reactions on Fe. The difference spectrum gives a visual indication of the observed precessions. The 221 keV line which depopulates the 221 keV state in  $^{81}\text{Sr}$  was one of primary interest. The other lines that show large effects are the 211 and 244 keV lines from  $^{82}\text{Y}$  and the 455 keV line, which is the  $2_1^+ \rightarrow 0_1^+$  transition in  $^{78}\text{Kr}$ . The region near 153 keV contains several lines from  $^{78}\text{Rb}$  and other nuclei, so the observed effects in the difference spectrum cannot be assigned unambiguously.

parameters are  $N_0$ ,  $\epsilon_i(E_{\gamma_1})$ ,  $\epsilon_j(E_{\gamma_2})$  and  $\sigma/I$ . (See Sections 5.1–5.3.)

The second mode of operation fits the full perturbed directional correlations for the two field directions simultaneously, namely

$$N_{ij}(+) = N_0 \epsilon_i(E_{\gamma_1}) \epsilon_j(E_{\gamma_2}) W(\theta_i, \theta_j, +) \quad (13)$$

and

$$N_{ij}(-) = N_0 R_{\pm} \epsilon_i(E_{\gamma_1}) \epsilon_j(E_{\gamma_2}) W(\theta_i, \theta_j, -) \quad (14)$$

where  $R_{\pm}$  is a parameter which takes into account any difference in the total beam intensity delivered for the two field directions. Again  $N_0$ ,  $\epsilon_i(E_{\gamma_1})$ ,  $\epsilon_j(E_{\gamma_2})$  and  $\sigma/I$  can be varied.  $W(\theta_i, \theta_j, \pm)$  also depends on the perturbations of the nuclear levels in and above the selected cascade.

Explicit expressions for  $W(\theta_i, \theta_j, \pm)$  in the special case of a three-level sequence  $I_1 \rightarrow I_2 \rightarrow I_3$  with no unobserved intermediate transitions were

given in Paper I. The computer code, however, uses an algorithm to evaluate the more general case which is illustrated on the left side of Fig. 15. A general cascade of arbitrary length can be specified between the two observed  $\gamma$  rays. The simplifying assumptions are that (i) the feeding precession  $\Delta\theta_{\text{feed}}$  is treated as a small, pure-magnetic perturbation, and (ii) only the last of the intermediate states experiences a perturbation, but this can be a magnetic perturbation of any magnitude, or a combined electric-quadrupole and magnetic-dipole interaction. This form is sufficiently general for the cases studied to date. On the one hand, for cascades involving a long-lived state, like the  $2_+$  state in the  $^{184}\text{Pt}$  example, the perturbation of this long-lived state dominates. Small corrections for the effects of any other intermediate states can easily be included manually, if required. On the other hand, when only

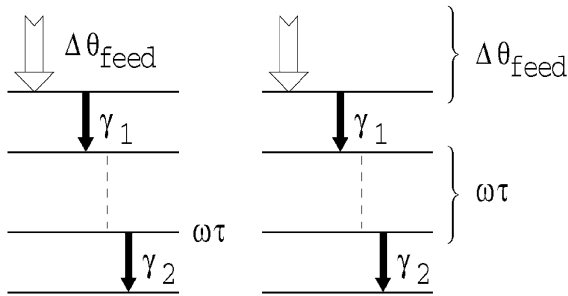


Fig. 15. The PDCO data can be analyzed in many cases in terms of the situation shown on the left. The level sequence and  $\gamma$ -ray cascade are general, but the perturbations are restricted to (i) a contribution inherited from above,  $\Delta\theta_{\text{feed}}$ , and (ii) that which takes place in the last of the intermediate states,  $\omega\tau$ . This case has wide applications because when the precessions are all small,  $<0.1$  rad, it is equivalent to the case shown on the right, i.e.  $\Delta\theta_{\text{feed}}$  is the net precession of the first state and  $\omega\tau$  is the net precession of the intermediate states.

small magnetic perturbations are encountered (as in the high-spin study on the Pt isotopes), the PDCO for the situation shown on the left of Fig. 15 is equivalent to that shown on the right. In other words,  $\Delta\theta_{\text{feed}}$  becomes the sum of the high-spin transient-field precession inherited by the upper state and the static-field precession taking place in the upper state itself, and  $\omega\tau$  becomes the total static-field precession accumulated in the intermediate states.

Fitting the full PDCO function to determine  $\omega\tau$  is most appropriate when  $\omega\tau \gtrsim 0.1$  rad. This procedure has therefore been used primarily to extract the precessions of the  $2^+$  states. The example shown in Fig. 16 is for the  $6^+ \rightarrow 4^+ \rightarrow 2^+ \rightarrow 0^+$  cascade in  $^{184}\text{Pt}$ , where the  $6^+ \rightarrow 4^+$  and  $2^+ \rightarrow 0^+$  transitions are detected. Since the information is spread over 84 data points, the plot may give the impression that the precession is not well determined; in fact the intermediate-state precession angle extracted from this data has an uncertainty of the order of 10%. Specifically, the fit in Fig. 16 gives a magnetic precession angle of  $\omega\tau = 0.29(2)$  rad and an electric quadrupole precession of  $\omega_Q\tau = 0.08(1)$  rad. A measure of  $\omega\tau(2^+)$  can also be obtained from all other cascades that include the  $2^+ \rightarrow 0^+$  transition.

### 5.7. Precessions from double-ratios

For small precessions,  $\omega\tau < 0.1$  rad, like those due to the transient-field effect at high spin, the use of a ratio-based analysis is imperative [4]. We have implemented two ways of determining the precession angles by forming double ratios, which factor out the detector efficiencies and the ratio between counting times for the two magnetic field directions. In both cases, the present computer code can vary  $\sigma/I$ ,  $\Delta\theta_{\text{feed}}$ ,  $\omega\tau$  and  $\omega_Q\tau$ ; however experience has shown that ratio data are not sensitive to  $\sigma/I$  and that it should therefore be evaluated from the unperturbed DCO data, as described above.

One way of forming a double ratio is as follows: if we denote the PDCO function by  $W(\theta_1, \theta_2, \pm)$  where the angle  $\theta_1$  denotes the angle of detection of the first transition (e.g.  $4^+ \rightarrow 2^+$ ) and  $\theta_2$  denotes that for the second transition (e.g.  $2^+ \rightarrow 0^+$ ) and  $\pm$  indicates the field direction, then double ratios can be formed for each two-detector combination ( $i, j$ ), where  $i$  and  $j$  now denote the detector numbers in Fig. 2 and Table 1:

$$\rho_{ij} = \sqrt{\frac{W(\theta_i, \theta_j, +)W(\theta_j, \theta_i, -)}{W(\theta_i, \theta_j, -)W(\theta_j, \theta_i, +)}}. \quad (15)$$

In other words, this double ratio involves just one pair of detectors and interchanges the angles at which the first and second transitions are detected.

It is usual to work with the ‘effect’,  $\varepsilon_{ij}$ , related to the double ratio  $\rho_{ij}$  by

$$\varepsilon_{ij} = (1 - \rho_{ij})/(1 + \rho_{ij}). \quad (16)$$

The precessions are then extracted by a simultaneous fit to the 21 independent  $\varepsilon_{ij}$  values involving all detector combinations, with the PDCO function  $W(\theta_1, \theta_2, \pm)$  evaluated as described above.

Another way of forming double ratios that exploits the fact that the angles in CAESAR are placed symmetrically about the beam axis, and is more akin to the standard IMPAC technique [4], is to define

$$R_{jk}^i = \sqrt{\frac{W(\theta_i, \theta_j, +)W(\theta_i, \theta_k, -)}{W(\theta_i, \theta_j, -)W(\theta_i, \theta_k, +)}} \quad (17)$$

where  $\theta_i$  is the angle at which the first  $\gamma$  ray is detected and the second  $\gamma$  ray is detected either in

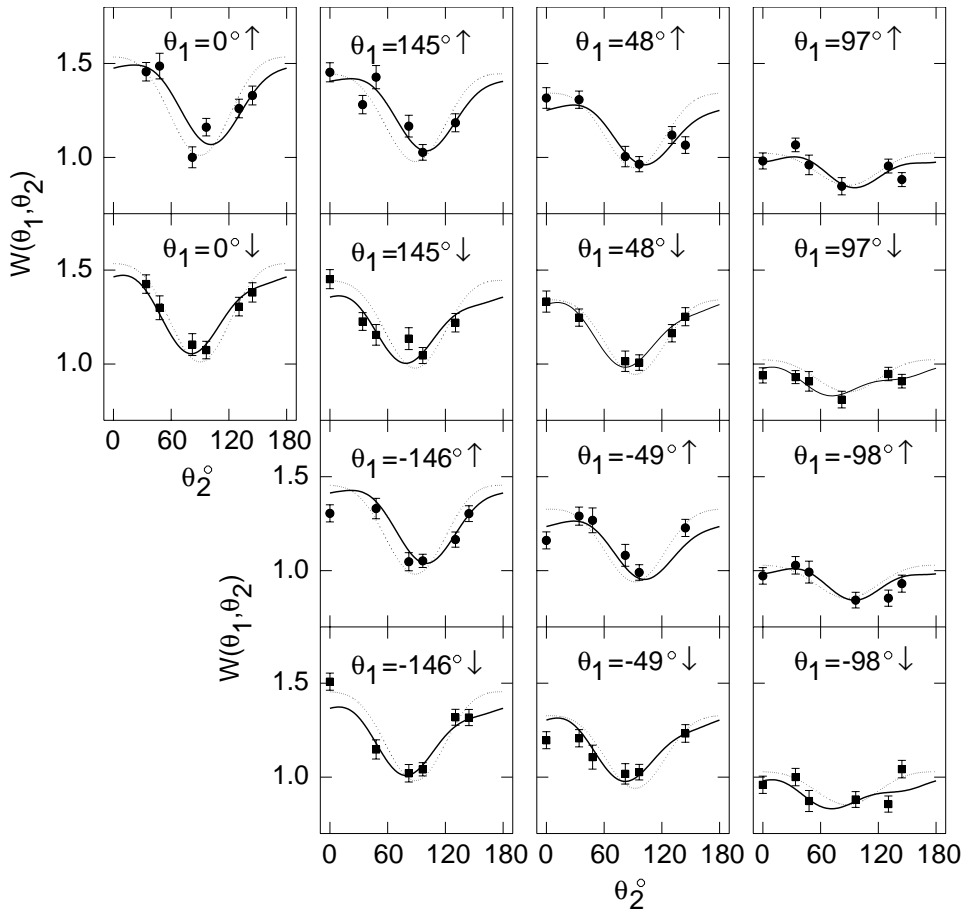


Fig. 16. Perturbed DCO for the  $6^+ \rightarrow 4^+ \dots 2^+ \rightarrow 0^+$  cascade in  $^{184}\text{Pt}$  (data points and solid lines), i.e. the  $6^+ \rightarrow 4^+$  transition is detected at angle  $\theta_1$  and the  $2^+ \rightarrow 0^+$  transition is detected at angle  $\theta_2$ . The intermediate  $4^+ \rightarrow 2^+$  transition is not observed. The unperturbed DCO is indicated by the dotted line. These data were fitted simultaneously and include the effect of an electric field gradient along with the magnetic interaction.

the detector at  $\theta_j$ , or the detector at  $\theta_k$ . Where possible,  $\theta_j$  and  $\theta_k$  correspond to a pair of detectors symmetrically placed on either side of the beam axis, i.e.  $\theta_k \simeq -\theta_j$ . When the first  $\gamma$  ray is detected at  $\theta_i = 0^\circ$  (i.e. in detector number 7), there are three independent double ratios:  $R_{14}^7$ ,  $R_{25}^7$  and  $R_{36}^7$ . In the other cases, where  $\theta_i \neq 0^\circ$ , three double ratios can still be formed, but only two have  $\theta_j \simeq -\theta_k$ , and one has  $\theta_j = 0^\circ$  and  $\theta_k = -\theta_i$  (or vice versa). For example, if the first transition is detected in detector number 1, the three independent ratios are  $R_{74}^1$ ,  $R_{25}^1$  and  $R_{36}^1$ . In all, there are 21 independent  $R_{jk}^i$  combinations and, again, we define the corresponding ‘effect’ values,

$\varepsilon_{jk}^i = (1 - R_{jk}^i)/(1 + R_{jk}^i)$ , and fit them simultaneously. This is our preferred method of forming double ratios because the selection of detectors placed symmetrically either side of the beam axis helps reduce systematic errors (e.g. like those that might arise from a displacement of the target with respect to the centre of the array).

An example of double-ratio data for the  $10^+ \rightarrow 8^+ \dots 6^+ \rightarrow 4^+$  cascade in  $^{184}\text{Pt}$ , presented as  $\varepsilon_{jk}^i$ , is given in Fig. 17. A fit to such data can give two experimental quantities: (i) the net precession of the  $10^+$  state (due to feeding and in the state itself), and (ii) the total static-field precession accumulated in the  $8^+$  and  $6^+$  states. This latter

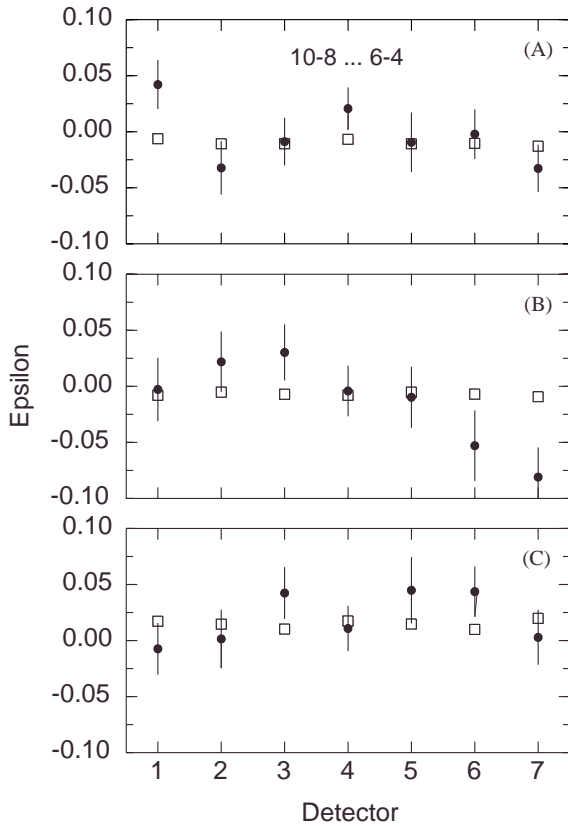


Fig. 17. Experimental and fitted epsilon values  $\epsilon_{jk}^i$  (see discussion of Eq. (17) in text) for the coincidence between the  $10^+ \rightarrow 8^+$  transition and the  $6^+ \rightarrow 4^+$  transition in  $^{184}\text{Pt}$ . The 21 independent experimental epsilon values (shown as data points with error bars) were fitted simultaneously. Calculated epsilon values that correspond to the best global fit are indicated by the open squares. In all cases the  $10^+ \rightarrow 8^+$  transition is recorded in the detector designated on the x-axis. In the upper (A), middle (B) and lower (C) panels the double ratios mainly involve the detection of the  $6^+ \rightarrow 4^+$  transition in the pairs of detectors near  $\pm 145^\circ$ ,  $\pm 97^\circ$  and  $\pm 49^\circ$ , respectively. When the  $10^+ \rightarrow 8^+$  transition is detected in one of the pair at  $\pm \theta$ , i.e.  $\theta_i \neq 0^\circ$ ,  $\epsilon_{jk}^i$  is formed with the  $6^+ \rightarrow 4^+$  transition detected at  $0^\circ$  (detector 7). See text for further details.

quantity is very small and the fits are not very sensitive to its precise value. In the final analysis of the high-spin transient-field precessions, the small static-field contributions were therefore fixed to reasonable calculated values (cf. Table 3).

Each of the analysis procedures described here involves a global fit to the whole data set. We note that a global fit method using the perturbed

angular-distribution formalism has been discussed recently by Weissman et al. [72]. Their concept is similar to our double-ratio analysis, although they use only a ‘single ratio’ of peak intensities for the two field directions.

Since the different analysis procedures discussed in this and the previous subsection combine the same data in different ways, they should yield consistent precession angles. However, depending on the magnitude of the precession, one method may be more appropriate, and hence more precise, than another. For example, a global fit to the PDCO function for the  $4^+ \rightarrow 2^+ \rightarrow 0^+$  transition in  $^{182}\text{Pt}$  gives  $\omega\tau(2^+) = 0.255(24)$  rad, whereas a double-ratio analysis of the same data gives  $\omega\tau(2^+) = 0.275(31)$  rad, which has a larger uncertainty because some information about the PDCO function has been lost in the formation of the ratios.

## 6. Applications to $g$ factors at high and low spin

In this section, we present some further aspects of the  $g$  factor measurements at high spin and low spin, including some results. It is beyond the scope of the present paper to discuss the experimental particulars and results in detail. The purpose here is to draw attention to the potential of the technique and to show consistency with previous data, where it exists. Further details of these measurements will be published in due course, e.g. Ref. [73].

### 6.1. High spin

The average high-spin  $g$  factors in  $^{180}\text{Pt}$ ,  $^{182}\text{Pt}$  and  $^{184}\text{Pt}$  were measured using the PDCO technique and transient fields. By measuring the precessions inherited by the discrete states at lower spin, this technique determines the average  $g$  factor at high spin ( $I \gtrsim 20\hbar$ ) in the discrete bands and the damping region of the continuum (see, e.g. [29,33,34,36] and references therein).

Several aspects of this measurement have been presented and discussed above. For example, some of the unperturbed DCO data are shown in Fig. 12 and an example from the ‘effect’ data is given in

Fig. 17. A subset of the data used to determine the transient-field precession of the high-spin quasicontinuum in  $^{184}\text{Pt}$  is shown in Table 4, along with details of the static-field contributions included in the analysis. These static-field corrections were proved to be of minor importance by another analysis of the data which ignored all static-field effects and yet yielded essentially the same value for the quasicontinuum  $g$  factor. The final high-spin  $g$  factor results for  $^{180}\text{Pt}$ ,  $^{182}\text{Pt}$  and  $^{184}\text{Pt}$  are summarized in Table 5.

It must be recognized that these experimental  $g$  factors are extracted from the data in a way that is not dependent on the entry-spin distribution of the reaction or the lifetimes of the states in the quasicontinuum. The interpretation of the data does, however, require an evaluation of such quantities.

Within errors, the average quasicontinuum  $g$  factors in  $^{180}\text{Pt}$ ,  $^{182}\text{Pt}$  and  $^{184}\text{Pt}$  are the same and are larger than the measured values of  $g(2_1^+)$ ; see below and Refs. [46,50,73]. This is in marked contrast with the previous measurements

[29,33,34,36] of average continuum  $g$  factors for even nuclei with  $70 \leq Z \leq 80$ , as summarized in Fig. 18. The smaller average  $g$  factors at high spin, usually in the range between 55% and 60% of  $Z/A$ , and with typical values of  $\langle g \rangle \sim 0.22$ , have been attributed to the rotational alignment of quasineutron configurations [29,33,34,36]. The  $\langle g \rangle$  values for the Pt isotopes point to contributions from aligned quasiproton configurations, along with the usual neutron alignment. Indeed a low- $K$   $\pi h_{9/2} \otimes i_{13/2}$  band becomes yrast at  $I \sim 25\hbar$  in both  $^{182}\text{Pt}$  and  $^{184}\text{Pt}$  [67,71].

Table 5

Measured precessions and average  $g$  factors in the high-spin quasicontinuum in  $^{180,182,184}\text{Pt}$

Isotope	Probe states	$\Delta\theta_{\text{feed}}$ (mrad)	$\langle g \rangle$
$^{180}\text{Pt}$	$6^+ - 10^+$	$-57 \pm 11$	$+0.40 \pm 0.08$
$^{182}\text{Pt}$	$6^+ - 12^+$	$-51 \pm 7$	$+0.36 \pm 0.05$
$^{184}\text{Pt}$	$6^+ - 14^+$	$-52 \pm 7$	$+0.37 \pm 0.05$

Table 4

Transient-field precessions feeding cascades in  $^{184}\text{Pt}$

$I_1 \rightarrow I_2^a$	$I_3 \rightarrow I_4^a$	$\omega\tau^b$ (mrad)	$\Delta\theta_{\text{feed}} + \omega\tau_{\text{feed}}^c$ (mrad)	$\omega\tau_{\text{feed}}^d$ (mrad)	$\Delta\theta_{\text{feed}}^e$ (mrad)
$10^+ \rightarrow 8^+$	$8^+ \rightarrow 6^+$	1.7(0.2)	−46(24)		
$10^+ \rightarrow 8^+$	$6^+ \rightarrow 4^+$	6.5(0.9)	−56(23)		
$10^+ \rightarrow 8^+$	$4^+ \rightarrow 2^+$	26.4(3.5)	−71(22)		
			$\langle -59(13) \rangle^f$	3.3(0.4)	−62(13)
$8^+ \rightarrow 6^+$	$6^+ \rightarrow 4^+$	4.8(0.6)	−45(18)		
$8^+ \rightarrow 6^+$	$4^+ \rightarrow 2^+$	24.7(3.3)	−32(19)		
			$\langle -39(13) \rangle^f$	5.0(0.7)	−44(13)
$6^+ \rightarrow 4^+$	$4^+ \rightarrow 2^+$	19.9(2.6)	−41(14)	9.8(1.3)	−50(14)
					$\langle -52(8) \rangle^f$

<sup>a</sup> First ( $I_1 \rightarrow I_2$ ) and second ( $I_3 \rightarrow I_4$ ) observed transitions.

<sup>b</sup> Estimated static-field precession of intermediate states. These values are included as a fixed input when fitting the experimental data.

<sup>c</sup> Measured total precession of the level  $I_1$ , including the precession of the states that feed it. These experimental values were obtained from fits to double-ratio data as described in the text.  $\Delta\theta_{\text{feed}}$  is the transient-field contribution and  $\omega\tau_{\text{feed}}$  is the static-field contribution.

<sup>d</sup> Estimated static-field contribution to the observed feeding precession, which is mainly due to the static-field precession in the state  $I_1$ .

<sup>e</sup> Experimental transient-field precession due to states in the quasicontinuum.

<sup>f</sup> Weighted average.

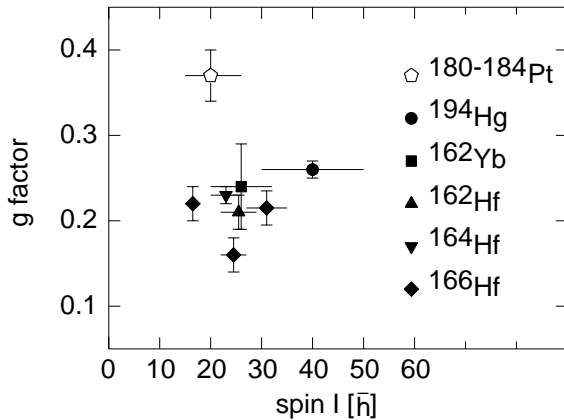


Fig. 18. Comparison between the average quasicontinuum  $g$  factors previously measured [29,33,34,36] in even nuclei with  $70 \leq Z \leq 80$  and the present result for  $^{180,182,184}\text{Pt}$ . The horizontal lines associated with the data points indicate the approximate range of spins sampled. In contrast with the other cases in this region, where quasineutron configurations reduce the high-spin  $g$  factor, quasiproton alignments are important, along with the usual neutron alignments, in the high-spin quasicontinuum of  $^{182}\text{Pt}$  and  $^{184}\text{Pt}$ .

## 6.2. Low spin

A preliminary account of the PDCO measurement on  $^{81}\text{Sr}$  has been given in Ref. [3]. Further experimental work, to determine more precisely the hyperfine field of Sr in Fe and the lifetime of the  $3/2^+$  state at 221 keV (previously determined as  $B_{\text{st}} = 10(3)$  T [5] and  $\tau = 0.91(29)$  ns [74], respectively), is currently underway.

As a by-product of the  $^{81}\text{Sr}$  measurement,  $^{78}\text{Kr}$  was populated relatively strongly. Although the  $2_1^+$  level lifetime in  $^{78}\text{Kr}$ ,  $\tau = 34.5(19)$  ps [75], is near the lower limit of those for which the technique was devised, an analysis of the 664–455 keV,  $4^+ \rightarrow 2^+ \rightarrow 0^+$  cascade in  $^{78}\text{Kr}$  gives  $\omega\tau = 35(13)$  mrad, which together with  $g = 0.43(3)$  [26], implies  $B_{\text{st}}(\text{KrFe}) = +49(19)$  T. This result for the static-field strength experienced by Kr impurities in Fe is of comparable precision to the value in the literature, namely  $+66(27)$  T [5]. If the new lifetime value,  $\tau = 27.5(25)$  ps, given in Ref. [26] is adopted, we get  $B_{\text{st}}(\text{KrFe}) = +61(24)$  T, which is in even better agreement with the literature value. (See note added in proof.)

The measurements on the platinum isotopes  $^{180,182,184}\text{Pt}$  were aimed primarily at developing the technique for heavy nuclei and measuring the relative  $g$  factors of the  $2^+$  states. However, precessions were also obtained for the  $4^+$  states, albeit with lower precision ( $\sim 50\%$ ). Despite the lower precision, these data have important implications for characterizing the hyperfine fields experienced by the implanted Pt nuclei in the Gd host. If pure magnetic interactions are assumed, the apparent static fields experienced by the  $2^+$  and  $4^+$  states are disparate by almost a factor of two. This contradiction can be resolved, and the present data brought into harmony with the previous static-field measurement [60], by recognizing that the longer-lived  $2^+$  states have time to respond to the electric-field gradient in the Gd host, along with the magnetic-dipole interaction, whereas the short-lived  $4^+$  states effectively only experience the magnetic interaction. This interpretation differs from a previous approach which attributed reduced magnetic interactions for Pt in Gd to there being a large fraction of implanted nuclei on field-free sites [50].

Analysis of the data on the  $2^+$  states must take into account the effects of the combined electric and magnetic interactions, which also offers the possibility of extending the technique to measure electric quadrupole moments. This aspect will be discussed in detail elsewhere [2].

The fit shown in Fig. 16 for the  $6^+ \rightarrow 4^+ \rightarrow 2^+ \rightarrow 0^+$  cascade in  $^{184}\text{Pt}$ , where the  $6^+ \rightarrow 4^+$  and  $2^+ \rightarrow 0^+$  transitions are detected, correctly takes into account the combined electric and magnetic interactions. The extracted value of the intermediate state precession is  $\omega\tau = 0.29(2)$  mrad. Taking  $B = -38(5)$  T and  $\tau = 543(13)$  ps yields  $g(2^+) = 0.27(4)$  after making a small correction for the precession of the  $4^+$  state. This result is in excellent agreement with the previous measurement,  $g(2^+) = 0.28(3)$ , which used the implantation-decay technique and an iron host [46]. Since states in  $^{180}\text{Pt}$ ,  $^{182}\text{Pt}$  and  $^{184}\text{Pt}$  were populated simultaneously in the present measurement, all the nuclei experience the same hyperfine fields, and relative  $g$  factors can be obtained for the three isotopes. The absolute  $g$  factors can be normalized to either the previous

value for the  $2^+$  state in  $^{184}\text{Pt}$  [46], or evaluated using the previously measured value of the hyperfine field of Pt in Gd [60]. In either case, the absolute values are very similar. The previous  $g(2^+)$  measurement provides a slightly more precise normalization.

Fig. 19 shows that the low-spin  $g$  factors extracted from the PDCO data for  $^{180,182,184}\text{Pt}$  are consistent with previous measurements [46,50], and generally support a shape-coexistence model of the  $g$  factors, as described in Ref. [46]. The smallest  $2^+$  state  $g$  factor in the platinum

isotopes is observed at the mid-shell nucleus  $^{182}\text{Pt}$  ( $N = 104$ ), where the number of valence neutrons is maximized, as is predicted by the lowest-order estimate of the Interacting Boson Model (see Ref. [46]). (Since this result depends on a previously measured lifetime for the  $2^+_1$  state in  $^{182}\text{Pt}$  that has not formally been published [76], a new measurement by direct timing techniques is in progress [77].)

## 7. Summary and concluding comments

We have described a technique for measuring the  $g$  factors of sub-nanosecond excited nuclear states based on the measurement of perturbed  $\gamma$ – $\gamma$  directional correlations following heavy-ion fusion–evaporation reactions. This technique should facilitate further measurements of  $g$  factors in neutron-deficient nuclei where the data for short-lived states are scarce. The technique is not subject to limitations from the beta-decay process as is the implantation-decay type of measurement [46], and is less beam-time intensive. For example, each measurement in Ref. [46] used about a week of beam time, whereas the present simultaneous measurements on  $^{180}\text{Pt}$ ,  $^{182}\text{Pt}$  and  $^{184}\text{Pt}$  were also done with about one week of beam time. An important advantage of the technique is that there are a number of redundancies in the data set that allow for internal consistency checks.

For wider applications to heavy nuclei, where Gd hosts are preferred to reduce unwanted beam-induced radiation, it may be necessary to more thoroughly characterize the hyperfine fields acting on nuclei implanted into these hosts.

Now that the technique has been developed, and experience in applying it has been gained, higher precision measurements can be planned for the future.

## Acknowledgements

The on-going support of the academic and technical staff of the Department of Nuclear Physics is gratefully acknowledged. We would like to thank A.B. Harding, Dr. D.C. Weissner and

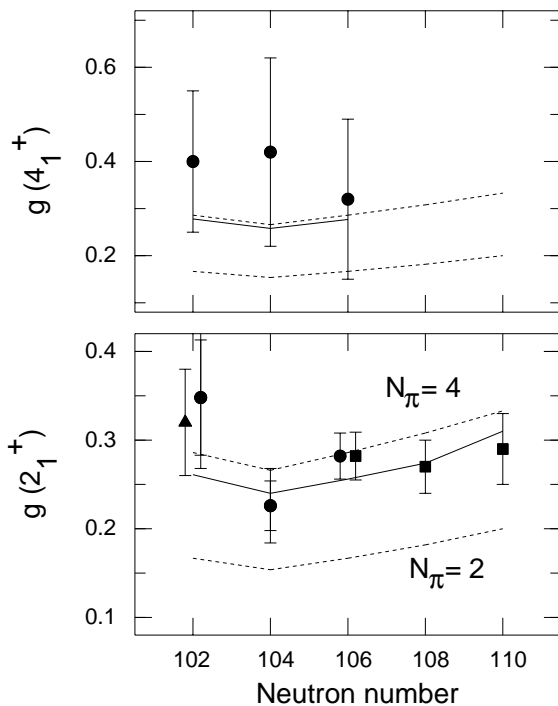


Fig. 19. Relative  $g$  factors of the lowest  $2^+$  and  $4^+$  states in  $^{180}\text{Pt}$ ,  $^{182}\text{Pt}$  and  $^{184}\text{Pt}$  from the present technique (circles), compared with previous results for  $^{180}\text{Pt}$  (triangle [50]),  $^{184}\text{Pt}$ ,  $^{186}\text{Pt}$ , and  $^{188}\text{Pt}$  (squares [46]). The absolute values of the present  $2^+$  results were obtained by normalizing to the previous  $g(2^+)$  value in  $^{184}\text{Pt}$  [46]. The two error limits on the present  $2^+$  results for  $^{180}\text{Pt}$  and  $^{182}\text{Pt}$  therefore indicate absolute and relative errors. The solid lines are theoretical estimates based on a shape-coexistence model in which the  $g$  factors of the deformed states are larger than that those of the near-spherical states. The Interacting Boson Model is used to estimate the  $g$  factors and the dotted lines show the  $g$  factors of the normal ( $N_\pi = 2$ ) and deformed ( $N_\pi = 4$ ) configurations.



A.J. Rawlinson for their contributions to the design and construction of apparatus. Our colleagues in the Nuclear Spectroscopy Group are thanked for their interest and assistance, especially Dr. A.N. Wilson who read and commented on the manuscript, and Dr. R.A. Bark who provided the diagram on which Fig. 2 is based.

### Note added in proof

Our discussion of the  $^{78}\text{Kr}$  data above was based on the hyper fine field for Kr in Fe given in the 1983 compilation of Ref. [5]. A more recent measurement [78] obtained  $B_{\text{st}}(\text{KrFe}) = +30.5(8)\text{ T}$ . For this field and  $\tau = 34.5(19)\text{ ps}$ , the measured precession of  $\omega\tau = 35(13)\text{ mrad}$  implies  $g(2^+) = 0.69(26)$ , which remains consistent with the transient field result [26].

### References

- [1] A.E. Stuchbery, M.P. Robinson, Nucl. Instr. and Meth. A 485 (2002) 753.
- [2] A.E. Stuchbery, M.P. Robinson, in preparation.
- [3] A.E. Stuchbery, Nucl. Phys. A 682 (2001) 470c.
- [4] N. Benczer-Koller, M. Hass, J. Sak, Ann. Rev. Nucl. Part. Sci. 30 (1980) 53.
- [5] K.S. Krane, Hyperfine Interactions 15/16 (1983) 1069.
- [6] G.N. Rao, Hyperfine Interactions 7 (1979) 141.
- [7] N.J. Stone, in: N.J. Stone, H. Postma (Eds.), Low-temperature Nuclear Orientation, North-Holland, Amsterdam, 1986 (Chapter 8).
- [8] H. Akai, M. Akai, S. Blügel, B. Drittler, H. Ebert, K. Terakura, R. Zeller, P.H. Dederichs, Prog. Theor. Phys. 101 (Suppl.) (1990) 11.
- [9] L. Grodzins, R. Borchers, G.B. Hagemann, Phys. Lett. 21 (1966) 214.
- [10] E. Recknagel, in: J. Cerny (Ed.), Nuclear Spectroscopy and Reactions, Part C, Academic Press, New York, 1974.
- [11] A.E. Stuchbery, A.G. White, G.D. Dracoulis, K.J. Schiffer, B. Fabricius, Z. Phys. A 338 (1991) 135.
- [12] A.E. Stuchbery, G.J. Lampard, H.H. Bolotin, Nucl. Phys. A 528 (1991) 447.
- [13] A.E. Stuchbery, S.S. Anderssen, H.H. Bolotin, A.P. Byrne, G.D. Dracoulis, B. Fabricius, T. Kibedi, Z. Phys. A 342 (1992) 373.
- [14] G.J. Lampard, A.E. Stuchbery, H.H. Bolotin, Nucl. Phys. A 536 (1992) 397.
- [15] G.J. Lampard, A.E. Stuchbery, H.H. Bolotin, S. Kuyucak, Nucl. Phys. A 568 (1994) 617.
- [16] S.S. Anderssen, A.E. Stuchbery, S. Kuyucak, Nucl. Phys. A 593 (1995) 212.
- [17] A.E. Stuchbery, G.J. Lampard, H.H. Bolotin, Nucl. Phys. A 642 (1998) 361.
- [18] M.P. Robinson, A.E. Stuchbery, E. Bezakova, S.M. Mullins, H.H. Bolotin, Nucl. Phys. A 647 (1999) 175.
- [19] E. Bezakova, A.E. Stuchbery, H.H. Bolotin, W.A. Seale, S. Kuyucak, P. Van Isacker, Nucl. Phys. A 669 (2000) 241.
- [20] A.E. Stuchbery, S.S. Anderssen, H.H. Bolotin, Nucl. Phys. A 669 (2000) 27.
- [21] P.F. Mantica, A.E. Stuchbery, D.E. Groh, J.I. Priscian-daro, M.P. Robinson, Phys. Rev. C 63 (2001) 034312.
- [22] K.-H. Speidel, N. Benczer-Koller, G. Kumbartzki, C. Barton, A. Gelberg, J. Holden, G. Jakob, N. Matt, R.H. Mayer, M. Satteson, R. Tanczyn, L. Weissman, Phys. Rev. C 57 (1998) 2181.
- [23] R. Ernst, K.-H. Speidel, O. Kenn, U. Hahum, J. Gerber, P. Maier-Komor, N. Benczer-Koller, G. Jakob, G. Kumbartzki, L. Zamick, F. Nowacki, Phys. Rev. Lett. 84 (2000) 416.
- [24] J. Holden, N. Benczer-Koller, G. Jakob, G. Kumbartzki, T.J. Mertzimekis, K.-H. Speidel, A. Macchiavelli, M. McMahan, L. Phair, P. Maier-Komor, A.E. Stuchbery, W.F. Rogers, A.D. Davies, Phys. Lett. B 493 (2000) 7.
- [25] J. Holden, N. Benczer-Koller, G. Jakob, G. Kumbartzki, T.J. Mertzimekis, K.-H. Speidel, C.W. Beausang, R. Krücken, A. Macchiavelli, M. McMahan, L. Phair, A.E. Stuchbery, P. Maier-Komor, W.F. Rogers, A.D. Davies, Phys. Rev. C 63 (2001) 024315.
- [26] T.J. Mertzimekis, N. Benczer-Koller, J. Holden, G. Jakob, G. Kumbartzki, K.-H. Speidel, R. Ernst, A. Macchiavelli, M. McMahan, L. Phair, P. Maier-Komor, A. Pakou, S. Vincent, W. Korten, Phys. Rev. C 64 (2001) 024314.
- [27] G. Jakob, N. Benczer-Koller, G. Kumbartzki, J. Holden, T.J. Mertzimekis, K.-H. Speidel, R. Ernst, A.E. Stuchbery, A. Pakou, P. Maier-Komor, A. Macchiavelli, M. McMahan, L. Phair, I.Y. Lee, Phys. Rev. C 65 (2002) 024316.
- [28] B. Skaali, R. Kalish, J. Eriksen, B. Herskind, Nucl. Phys. A 238 (1975) 159.
- [29] H.-E. Mahnke, O. Häusser, H. Grawe, H. Kluge, W. Semmler, Phys. Lett. B 134 (1984) 153.
- [30] O. Häusser, D. Ward, H.R. Andrews, P. Taras, B. Haas, M.A. Deleplanque, R.M. Diamond, E.L. Dines, A.O. Macchiavelli, R. McDonald, F.S. Stephens, C.V. Stager, Phys. Lett. B 144 (1984) 341.
- [31] P. Taras, O. Häusser, H.R. Andrews, D. Ward, M.A. Deleplanque, R.M. Diamond, A.O. Macchiavelli, F.S. Stephens, Nucl. Phys. A 435 (1985) 294.
- [32] M. Hass, N. Benczer-Koller, G. Kumbartzki, T. Lauritsen, T.L. Khoo, I. Ahmad, M.P. Carpenter, R.V.F. Janssens, E.F. Moore, F.L.H. Wolfs, Ph. Benet, K. Beard, Phys. Rev. C 44 (1991) 1397.
- [33] L. Weissman, M. Hass, C. Broude, Phys. Rev. C 53 (1996) 151.
- [34] L. Weissman, M. Hass, C. Broude, Phys. Rev. C 57 (1998) 621.

- [35] R.H. Mayer, G. Kumbartzki, L. Weissman, N. Benczer-Koller, C. Broude, J.A. Cizewski, M. Hass, J. Holden, R.V.F. Janssens, T. Lauritsen, I.Y. Lee, A.O. Macchiavelli, D.P. McNabb, M. Satteson, *Phys. Rev. C* 58 (1998) R2640.
- [36] L. Weissman, R.H. Mayer, G. Kumbartzki, N. Benczer-Koller, C. Broude, J.A. Cizewski, M. Hass, J. Holden, R.V.F. Janssens, T. Lauritsen, I.Y. Lee, A.O. Macchiavelli, D.A. McNabb, M. Satteson, *Phys. Lett. B* 446 (1999) 22.
- [37] C.G. Ryan, H.H. Bolotin, A.E. Stuchbery, Department of Nuclear Physics Annual Report, ANU-P/880, 1983, p. 54.
- [38] C.G. Ryan, Ph.D. Thesis, University of Melbourne, 1985, unpublished.
- [39] U. Birkental, A.P. Byrne, S. Heppner, H. Hübel, W. Schmitz, P. Fallon, P.D. Forsyth, J.W. Roberts, H. Kluge, E. Lubkiewicz, G. Goldring, *Nucl. Phys. A* 555 (1993) 643.
- [40] A. Jungklaus, C. Teich, V. Fischer, D. Kast, K.P. Lieb, C. Link, C. Ender, T. Härtlein, F. Köck, D. Schwalm, J. Billowes, J. Eberth, H.G. Thomas, *Phys. Rev. Lett.* 80 (1998) 2793.
- [41] C. Teich, A. Jungklaus, V. Fischer, D. Kast, K.P. Lieb, C. Link, C. Ender, T. Härtlein, F. Köck, D. Schwalm, J. Billowes, J. Eberth, H.G. Thomas, *Phys. Rev. C* 59 (1999) 1943.
- [42] A. Zemel, C. Broude, E. Dafni, A. Gelberg, M.B. Goldberg, J. Gerber, G.J. Kumbartzki, K.-H. Speidel, *Nucl. Phys. A* 383 (1982) 165.
- [43] J. Billowes, C.H. Holbrow, T. Lauritsen, K.P. Lieb, R.G. Pillay, S.L. Rolston, G.D. Sprouse, *Phys. Lett. B* 178 (1986) 145.
- [44] M. Weiszflog, J. Billowes, A. Herder, M.K. Kabadiyski, K.P. Lieb, J. Rudolph, T. Burkhard, J. Eberth, T. Mylaeus, S. Skoda, *J. Phys. G* 20 (1984) L77.
- [45] P.H. Regan, A.E. Stuchbery, S.S. Anderssen, *Nucl. Phys. A* 591 (1995) 533.
- [46] A.E. Stuchbery, S.S. Anderssen, A.P. Byrne, P.M. Davidson, G.D. Dracoulis, G.J. Lane, *Phys. Rev. Lett.* 76 (1996) 2246.
- [47] G. Menzen, A. Wolf, H. Lawin, G. Lhersonneau, K. Sistemich, *Z. Phys. A* 321 (1985) 593.
- [48] R.L. Gill, D.D. Warner, H. Mach, A. Piotrowski, A. Wolf, J.C. Hill, F.K. Wohn, J.A. Winger, B. Fogelberg, *Phys. Rev. C* 33 (1986) 1030.
- [49] A.G. Smith, G.S. Simpson, J. Billowes, J.L. Durell, P.J. Dagnall, S.J. Freeman, M. Leddy, A.A. Roach, J.F. Smith, A. Jungklaus, K.P. Lieb, C. Teich, B.J.P. Gall, F. Hoellinger, N. Schulz, I. Ahmad, J. Greene, A. Algora, *Phys. Lett. B* 453 (1999) 206.
- [50] F. Brandolini, N.H. Medina, A.E. Stuchbery, S.S. Anderssen, H.H. Bolotin, D. Bazzacco, D. De Acuña, M. De Poli, R. Menegazzo, P. Pavan, C. Rossi Alvarez, G. Vedovato, *Eur. Phys. J. A* 3 (1998) 129.
- [51] G.D. Dracoulis, A.P. Byrne, Department of Nuclear Physics Annual Report, Australian National University, ANU-P/1052, 1989, p. 115, unpublished.
- [52] A.B. Harding, M.P. Robinson, A.E. Stuchbery, D.C. Weissner, Department of Nuclear Physics Annual Report, Australian National University, ANU-P/1420, 1999, p. 122, unpublished.
- [53] A. Gavron, *Phys. Rev. C* 2 (1980) 230.
- [54] J.F. Ziegler, J.P. Biersack, U. Littmark, in: J.F. Ziegler (Ed.), *The Stopping and Ranges of Ions in Matter*, Pergamon, New York, 1985.
- [55] N.K.B. Shu, D. Melnick, J.M. Brennan, W. Semmler, N. Benczer-Koller, *Phys. Rev. C* 21 (1980) 1828.
- [56] S.S. Anderssen, A.E. Stuchbery, *Hyperfine Interactions* 96 (1995) 1.
- [57] A.E. Stuchbery, S.S. Anderssen, E. Bezakova, *Hyperfine Interactions* 97/98 (1996) 479.
- [58] A.E. Stuchbery, E. Bezakova, *Aust. J. Phys.* 51 (1998) 183.
- [59] A.E. Stuchbery, E. Bezakova, *Phys. Rev. Lett.* 82 (1999) 3637.
- [60] A.E. Stuchbery, S.S. Anderssen, *Phys. Rev. C* 51 (1995) 1017.
- [61] U. Garg, A. Chaudhury, M.W. Drigert, E.G. Funk, J.W. Mihelich, D.C. Radford, H. Helppi, R. Holzmann, R.V.F. Janssens, T.L. Khoo, A.M. van den Berg, J.L. Wood, *Phys. Lett. B* 180 (1986) 319.
- [62] M. Finger, R. Foucher, J.P. Husson, J. Jastrzebski, A. Johnson, G. Astner, B.R. Erdal, A. Kjelberg, P. Patzelt, A. Hoglund, S.G. Malmeskog, R. Henck, *Nucl. Phys. A* 188 (1972) 369.
- [63] A.E. Stuchbery, Computer Program PDCOFIT, unpublished.
- [64] T. Yamazaki, *Nucl. Data A* 3 (1967) 1.
- [65] A. Nordlund, *Nucl. Instr. and Meth. A* 368 (1996) 731.
- [66] S.S. Anderssen, Ph.D. Thesis, Australian National University, 1995, unpublished.
- [67] M.P. Carpenter, C.R. Bingham, L.H. Courtney, V.P. Janzen, A.J. Larabee, Z.-M. Liu, L.L. Riedinger, W. Schmitz, R. Bengtsson, T. Bengtsson, W. Nazarewicz, J.-Y. Zhang, J.K. Johansson, D.G. Popescu, J.C. Waddington, C. Baktash, M.L. Halbert, N.R. Johnson, I.Y. Lee, Y.S. Schutz, J. Nyberg, A. Johnson, R. Wyss, J. Dubuc, G. Kajrys, S. Monaro, S. Pilotte, K. Honkanen, D.G. Sarantites, D.R. Haenni, *Nucl. Phys. A* 513 (1990) 125.
- [68] L.V. Theisen, S.L. Tabor, L.R. Medsker, G. Neuschaefer, L.H. Fry Jr., J.S. Clements, *Phys. Rev. C* 25 (1982) 1325.
- [69] R.A. Bark, A.E. Stuchbery, A. Tulapurkar, M.P. Robinson, Department of Nuclear Physics Annual Report, Australian National University, ANU-P/1420, 1999, p. 28, unpublished.
- [70] J. Burde, R.M. Diamond, F.S. Stephens, *Nucl. Phys. A* 92 (1967) 306.
- [71] D.G. Popescu, J.C. Waddington, J.A. Cameron, J.K. Johansson, N.C. Schmeing, W. Schmitz, M.P. Carpenter, V.P. Janzen, J. Nyberg, L.L. Riedinger, H. Hübel, G. Kajrys, S. Monaro, S. Pilotte, C. Bourgeois, N. Perrin, H. Sergolle, D. Hojman, A. Korichi, *Phys. Rev. C* 55 (1997) 1175.

- [72] L. Weissman, M. Hass, N. Benczer-Koller, C. Broude, G. Kumbartzki, Nucl. Instr. and Meth. 416 (1998) 351.
- [73] M.P. Robinson, A.E. Stuchbery, R.A. Bark, A.P. Byrne, G.D. Dracoulis, S.M. Mullins, A.M. Baxter, Phys. Lett. B 530 (2002) 74.
- [74] S.E. Arnell, C. Ekström, L.P. Ekström, A. Nilsson, I. Ragnarsson, P.J. Smith, E. Wallander, J. Phys. G 9 (1983) 1217.
- [75] S. Rab, Nucl. Data Sheets 63 (1991) 1.
- [76] U. Garg, private communication; J.C. Walpe, U. Garg, S. Naguleswaran, W. Reviol, J. Wei, D. Ye, I. Ahmad, I. Bearden, M.P. Carpenter, R.V.F. Janssens, T.L. Khoo, T. Lauritsen, Bull. Am. Phys. Soc. 39 (1994) 1419.
- [77] A.N. Wilson, A.E. Stuchbery, P.M. Davidson, W.P.D. Mitchell, R.A. Bark, G.D. Dracoulis, P.F. Mantica, in preparation.
- [78] N. Severijns, J. Wouters, J. Vanhaverbeke, W. Vanderpoorten, L. Vanneste, Hyperfine Interactions 52 (1989) 831.